Chapter 1

Introduction

1.1 Angular Broadening, Pulse Broadening, and Scintillation

The dispersion relation for radiation of frequency ω propagating in a plasma is

$$\omega^2 - c^2 k^2 = \frac{4\pi N e^2}{m}, \tag{1.1}$$

where N is the number density of electrons, e is the electron charge, and m is the electron mass. The index of refraction n is therefore

$$n = \sqrt{1 - \frac{\omega_p^2}{\omega^2}} \tag{1.2}$$

where $\omega_p = \sqrt{4\pi N e^2 / m}$ is the plasma frequency. In the interstellar medium (ISM), the plasma frequency is of order 10^4 Hz, well below typical observing frequencies; hence, the ISM is transparent to radiation at these frequencies. Fluctuations in the electron density and hence the index of refraction, however, will scatter the radiation, resulting in angular broadening, pulse broadening, and interstellar scintillation.

While models of scattering in an extended medium have been explored, simplified models typically assume that radiation from a source scatters off of a thin

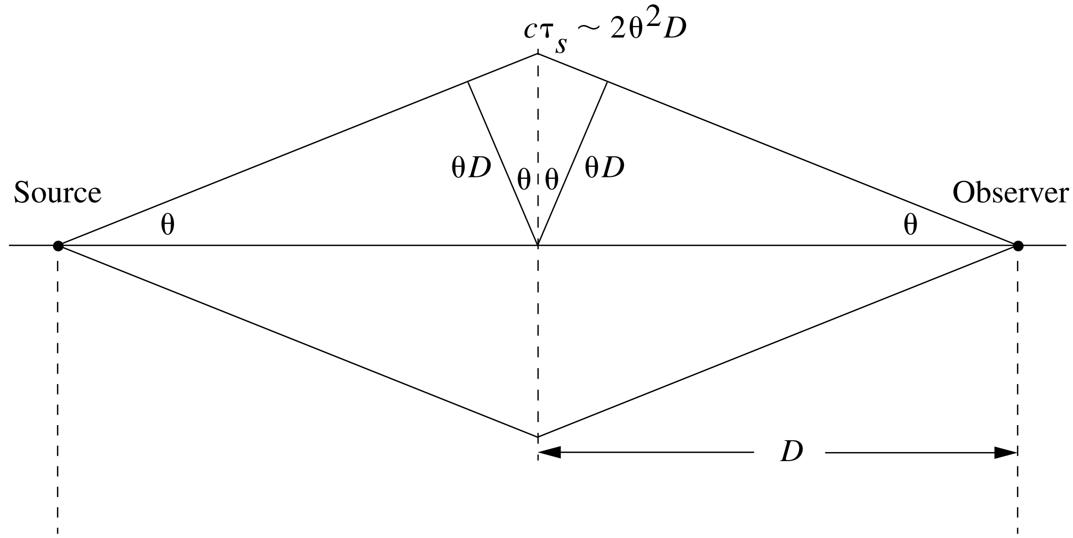

Figure 1.1— In a simplified model of scattering, radiation scatters off of a thin screen of material located midway between the source and observer. A δ-function emission from a point source reaches the observer over a range of angles and times, and interference between multiple rays results in the phenomenon of interstellar scintillation.

screen located between the source and the observer, as illustrated in Figure 1.1. Scattered radiation from a point source reaches the observer via multiple paths; consequently, the observer sees a broadened image, detecting radiation within a cone of angle θ. Furthermore, rays which travel directly from the source to observer arrive first while scattered rays traverse a longer distance and arrive later. A δ-function pulse emitted at the source, therefore, reaches the observer over a range of times, characterized by the pulse broadening time τ_s.

In addition to angular broadening and pulse broadening, scattering also causes interstellar scintillation. Interference among multiple rays creates a diffraction pattern in the observing plane, and the motion of the source and scattering screen causes the diffraction pattern to move relative to the observer with scintillation velocity V_{ISS}. Observers will therefore see the intensity of the source vary with time.

The scintillation time scale t_{ISS} reflects the typical size of a diffraction maximum in the observing plane. The scattering disk acts like a lens of angular size θ and produces diffraction-limited images of the pulsar in the observing plane with characteristic size of order λ / θ, where λ is the wavelength of the radiation. Because the diffraction pattern moves with speed V_{ISS}, an observer will, on average, detect a maximum for a length of time $t_{ISS} \sim \lambda / \theta V_{ISS}$. The scintillation time scale is traditionally measured as the time lag where the intensity autocorrelation function falls to e^{-1}.

The decorrelation bandwidth $\Delta\nu_{ISS}$ is the typical size of a diffraction maximum in the frequency domain. The diffraction maxima have finite widths because the conditions which result in constructive interference at one frequency will result in destructive interference at a sufficiently different frequency. Observationally, the decorrelation bandwidth is defined to be the half-width at half-maximum of the intensity autocorrelation function at zero time lag.

1.2 Uncertainty Relation

The decorrelation bandwidth and the pulse broadening are related via an uncertainty relation. The pulse-broadening delay τ_s corresponds to an additional distance $c\tau_s$ traversed by the scattered rays, and this extra distance translates into a phase difference of $2\pi c\tau_s / \lambda = 2\pi\nu\tau_s$, where $\nu = c / \lambda$ is the frequency of the radiation. Hence, the change in frequency needed to produce a phase difference of one radian is

$$\Delta\nu = \frac{1}{2\pi\tau_s}. \tag{1.3}$$

If the rays cohere at a frequency ν, then they will begin to decohere at frequency $\nu+\Delta\nu$. Hence, we can identify the phase change $\Delta\nu$ above with the decorrelation bandwidth $\Delta\nu_{ISS}$.

More generally, we can write

$$\Delta\nu_{ISS} = \frac{C_1}{2\pi\tau_s} \tag{1.4}$$

to allow for the various definitions of $\Delta\nu_{ISS}$ and τ_s. From their analysis of pulse propagation in the ISM, Lambert & Rickett (1999) derived a value of $C_1 = 0.654$ for a thin-screen geometry and a Kolmogorov turbulence spectrum, but they note that in the literature, stated values of C_1 range from 0.6 to 1.53 for this configuration.

1.3 Dispersion Measure and Temporal Broadening

The group velocity for a pulse propagating through the ISM is given by

$$v_g = \frac{d\omega}{dk} \cong c\left[1 - \frac{2\pi N e^2}{mc^2k^2}\right], \tag{1.5}$$

so the time T needed for a pulse to travel a distance L is

$$T = \int_0^L \frac{dl}{v_g} \cong \frac{L}{c} + \frac{2\pi e^2}{mc^3k^2}\int_0^L N(l)dl. \tag{1.6}$$

The first term is the travel time in a vacuum. The second term represents the delay due to the electrons. The integral in the second term is called the dispersion measure, or the total electron content, along the line of sight from the pulsar to the observer.

The characteristic angle θ_s through which a ray scatters predictably increases with distance and hence with dispersion measure. For a Gaussian turbulence spectrum, the density irregularities have a characteristic size a, and the number of these irregularities a ray passes through will be L / a, where L is the distance to the pulsar. So if a density irregularity typically deflects a ray by an angle $\delta\theta$, the scattering angle θ_s will be given by

$$\theta_s = \left(\frac{L}{a}\right)^{1/2} \delta\theta. \tag{1.7}$$

With a screen midway between the source and observer, the angular size of the source will be $\theta = \theta_s / 2$; hence, from Figure 1.1, we can see that the temporal broadening of the pulsar will be roughly

$$\tau_s \approx \frac{\theta^2 L}{c} = \frac{L^2}{4ac}\delta\theta^2. \tag{1.8}$$

If we assume that the electron density N is roughly constant, then the dispersion measure is proportional to L, and we find that $\tau_s \propto DM^2$. For a Kolmogorov spectrum, we expect $\tau_s \propto DM^{2.2}$ (Lee & Jokipii 1975).

Observation, however, shows that while for low dispersion measure, τ_s scales as expected, for large dispersion measures, $\tau_s \propto DM^{4.4}$, as shown in Figure 1.2. The cutoff between the two regimes appears to occur around $DM \sim 30 - 75$ cm^{-3} pc. Sutton (1971) first noted this discontinuity in scaling and attributed the change in

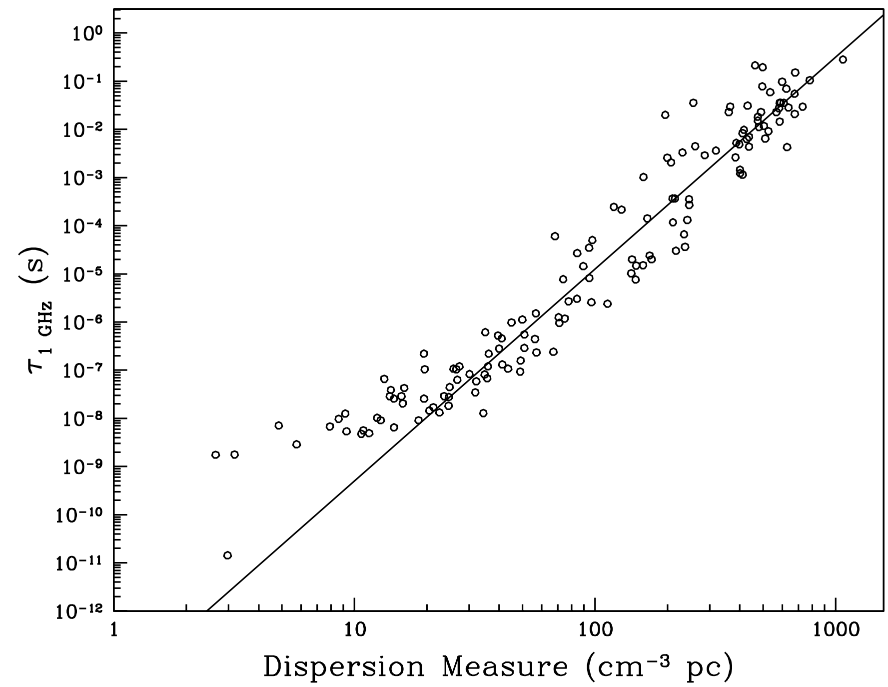

Figure 1.2— The observed relationship between temporal broadening and dispersion measure. The line, fit by eye, has a slope of 4.4, corresponding to a Kolmogorov turbulence spectrum. The data were taken from pulsar catalog compiled by Taylor, Manchester, & Lyne (1993).

power-law index at high dispersion measure to increased scattering of distant pulsars by HII regions.

One feature of the diagram provides an interesting clue. The temporal broadening of pulsars on the lower arm in the diagram is inferred via the uncertainty relation from measurements of the decorrelation bandwidth while for pulsars on the upper arm, it is determined by examining the pulse shape. This fact has focused some attention on the validity of the uncertainty relation. Rickett (1977), however, notes that “the theory [of interstellar scintillation] leaves very little flexibility.” The association between $\Delta\nu_{ISS}$ and τ_s is a generic feature of scattering models. Backer (1974), moreover, compared his measurement of $\Delta\nu_{ISS}$ for the Vela pulsar to a measurement of τ_s by Komesaroff, Hamilton, & Ables (1972) and confirmed the validity of the relationship between the decorrelation bandwidth and temporal broadening.

1.4 Electron Density Fluctuations

The autocorrelation function of the density fluctuations is the Fourier transform of the power spectrum:

$$\langle \Delta n(\mathbf{x}) \Delta n(\mathbf{x}+\mathbf{r}) \rangle = \int P(\mathbf{q}) e^{-i\mathbf{q}\cdot\mathbf{r}} d\mathbf{r}\,. \tag{1.9}$$

Here $\Delta n(\mathbf{x}) = n(\mathbf{x}) - \langle n(\mathbf{x}) \rangle$ where the brackets denote averaging over $\mathbf{x}$. In the Kolmogorov model, the power spectrum of the electron density fluctuations is given by

$$P(\mathbf{q}) = C_n^2 |\mathbf{q}|^{-11/3} \qquad \frac{2\pi}{l_o} \le |\mathbf{q}| \le \frac{2\pi}{l_i} \tag{1.10}$$

which holds between an inner length scale l_i and outer length scale l_o. C_n denotes the level of density fluctuations, and $\mathbf{q}$, the wave vector. Energy is injected into the ISM at the outer length scale. A turbulent cascade distributes this energy to smaller length scales until it reaches the inner length scale l_i, at which point the energy is dissipated into heat.

These fluctuations result in variations in the index of refraction. Because the observing frequency is much greater than the plasma frequency, we can expand equation (1.2) in a Taylor series to get

$$n = 1 - \frac{1}{2}\frac{\omega_p^2}{\omega^2} = 1 - \frac{1}{2}\frac{4\pi N e^2}{m\omega^2} = 1 - \frac{N r_e \lambda^2}{2\pi} \tag{1.11}$$

where $r_e = e^2 / mc^2$ is the classical radius of the electron. In terms of deviations about mean values of the electron density and index of refraction, we have

$$\Delta n = -\frac{\Delta N r_e \lambda^2}{2\pi}, \tag{1.12}$$

where $\Delta N = N - \langle N \rangle$ and $\Delta n = n - \langle n \rangle$. Propagation over a distance Δz therefore results in a phase change of

$$\Delta\phi = 2\pi\frac{\Delta z}{\lambda / n} = \frac{2\pi\Delta z\langle n \rangle}{\lambda} + \frac{2\pi\Delta z}{\lambda}\Delta n \tag{1.13}$$

The first term is the portion of the phase change due to propagating in a uniform medium while the second term is the contribution due to the density fluctuation. The total phase introduced by the density fluctuations in a screen of thickness Z is therefore

$$\Phi(\mathbf{x}) = -r_e\lambda\int_0^Z \Delta N(\mathbf{x}, z)dz. \tag{1.14}$$

Propagation through the screen also adds a phase due to the mean electron density; however, since we are concerned only with phase differences, we may neglect this constant contribution to the phase.

1.5 Scaling with Observing Frequency

For a Gaussian turbulence spectrum with characteristic width a, the phase fluctuation caused by a single irregularity, $\Delta\phi = a r_e \lambda \Delta N$, corresponds to a scattering angle of

$$\delta\theta = \frac{\Delta\phi}{2\pi}\frac{\lambda}{a} = \frac{1}{2\pi} r_e \lambda^2 \Delta N. \tag{1.15}$$

This result combined with equation (1.8) shows that $\tau_s \propto \nu^{-4}$, and from the uncertainty relation, we have $\Delta\nu_{ISS} \propto \nu^4$. For a Kolmogorov turbulence spectrum, we expect $\Delta\nu_{ISS}$ to scale as $\nu^{4.4}$ (Lee & Jokipii).

As we will see later, the scintillation velocity is given by

$$V_{ISS} = \frac{\sqrt{\Delta\nu_{ISS} L x (c / 2\pi)}}{\nu t_{ISS}}, \tag{1.16}$$

where x is a dimensionless parameter and L is the distance to the pulsar. The velocities of and distances to the pulsar and scattering screen determine the speed of the diffraction pattern; V_{ISS} does not depend on observing frequency. Using dimensional analysis, we can therefore deduce that for a Gaussian spectrum, $t_{ISS} \propto \nu$, and for a Kolmogorov spectrum, $t_{ISS} \propto \nu^{1.2}$.

1.6 Scattering by a Thin Screen

1.6.1 Phase-Changing Scattering Screen

Figure 1.3 depicts the geometry of scattering by a thin screen. In this model, the phase changes due to electron density fluctuations occur only within a thin screen located between the source and observer. The screen is thick enough so that many density fluctuations contribute to the phase added by the screen, so that the added phase can be considered a Gaussian random variable, regardless of the statistical characteristics of the density fluctuations. The screen, however, is thin enough so that we may neglect scattering within the screen.

1.6.2 Electric Field and Intensity in the Observing Plane

The electric field at a point **b** on the observing plane is given by

$$E(\mathbf{b}) = E_s \int \frac{e^{ik\sqrt{R^2 + \mathbf{x}^2}}}{\sqrt{R^2 + \mathbf{x}^2}} e^{i\Phi(\mathbf{x})} \frac{e^{ik\sqrt{D^2 + (\mathbf{x} - \mathbf{b})^2}}}{\sqrt{D^2 + (\mathbf{x} - \mathbf{b})^2}} d\mathbf{x}, \tag{1.17}$$

where E_s is the electric field at the pulsar, which we assume is a point source, k is the wave number, R is the distance from the pulsar to the scattering screen, and D is the distance from the scattering screen to the observing plane. The first factor in the integrand represents propagation from the pulsar to a point **x** on the scattering screen; the second factor, propagation through the scattering screen; and the final factor,

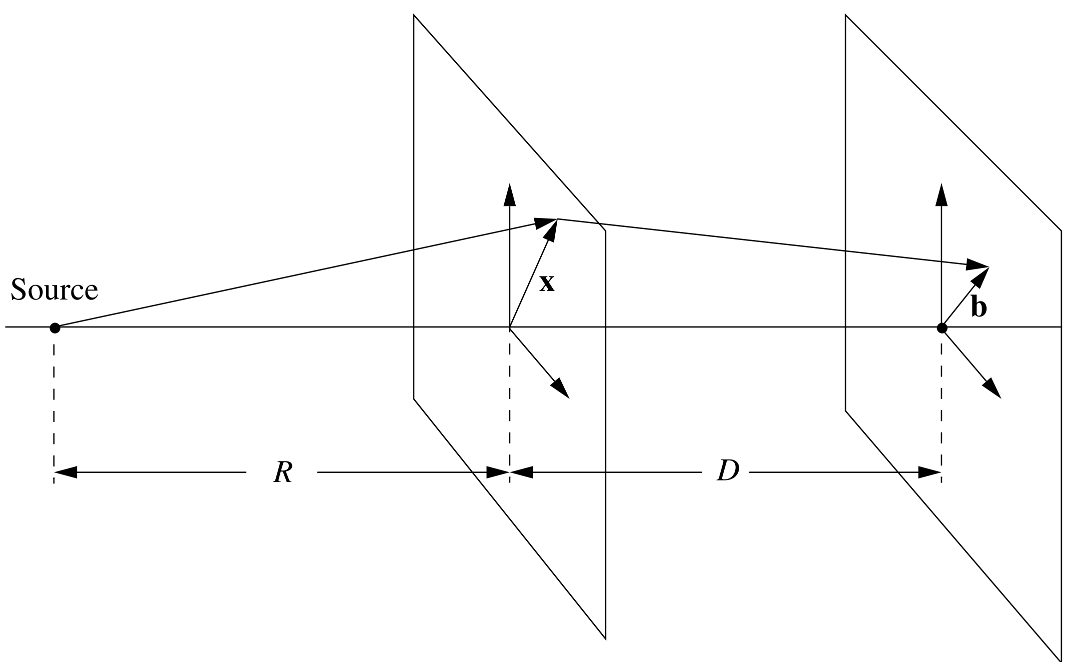

Figure 1.3— Thin-screen scattering geometry. Radiation from a point source scatters at point **x** on the scattering screen and reaches the observing plane at point **b**.

propagation from the point $\mathbf{x}$ on the scattering screen to the point $\mathbf{b}$ on the observing plane. The electric field at a point $\mathbf{b}$ on the observing plane is then the phasor sum of the contributions from each point on the scattering screen.

Because the distances R and D are much greater than the lateral distances $|\mathbf{x}|$ and $|\mathbf{b}|$, we may expand the radicals in the exponents to first order to get

$$\begin{aligned} E(\mathbf{b}) &= \frac{E_s e^{ik(D + R + \mathbf{b}^2 / D)}}{RD} \int \exp\left\{\frac{ik}{2}\left[\left(\frac{1}{R} + \frac{1}{D}\right)\mathbf{x}^2 + \frac{2\mathbf{x} \cdot \mathbf{b}}{D}\right] + i\Phi(\mathbf{x})\right\} d\mathbf{x} \\ &= E_0 \int \exp\left[ik\frac{\mathbf{x} \cdot \mathbf{b}}{D} + i\phi(\mathbf{x})\right] d\mathbf{x} \end{aligned} \tag{1.18}$$

The complex constant E_0 consolidates the constant terms in front of the integral and absorbs the terms of constant phase, and $\phi(\mathbf{x})$ combines the baseline-independent portion of the geometric phase, $k(1/2R + 1/2D)\mathbf{x}^2$, and the screen phase, $\Phi(\mathbf{x})$.

If the phase of the integrand varies rapidly, the integral averages to almost zero, and the non-cancelling contributions to the integral arise from so-called stationary points, points where the phase of the integrand reaches an extremum. In this case, we can approximate the integral as a sum over these stationary points:

$$E(\mathbf{b}) = E_0 \sum_j \frac{1}{H_j} \exp\left(ik\frac{\mathbf{x}_j \cdot \mathbf{b}}{D} + i\phi_j\right), \tag{1.19}$$

where $\phi_j = \phi(\mathbf{x}_j)$ and the factor H_j accounts for the sharpness of the extremum at $\mathbf{x}_j$.

The distribution of these stationary points defines the extent of the scattering disk. For large $|\mathbf{x}|$, the parabolic term increases so quickly that the variations in the screen phase are unlikely to produce extrema, thus limiting the size of the scattering disk. In the thin-screen model, we assume that a ray encounters many density fluctuations; hence, the central limit theorem ensures that the screen phase $\Phi(\mathbf{x})$ is a Gaussian random variable. Because the angle through which a ray is deflected is proportional to this phase, the angular distribution of a source is also Gaussian. It follows then that the distribution of stationary points, with weightings H_j^{-2}, follows the normal distribution

$$P(\mathbf{x}) = \frac{1}{2\pi r_R^2} e^{-\frac{\mathbf{x}^2}{2r_R^2}} \tag{1.20}$$

where $r_R = \theta D$ is the characteristic size of the scattering disk.

In addition to the refractive scale r_R, two other distance scales enter into the description of the scattering process. The distance r_d characterizes the scattering screen; it is the distance over which the phase of the screen will typically vary by a radian. And the Fresnel distance $r_F = [k(1/2R + 1/2D)]^{1/2}$ sets the scale for the geometric phase. In the strong scattering regime, we have $r_d \ll r_F \ll r_R$. The screen phase varies rapidly within a Fresnel zone, and the scattering disk contains many Fresnel zones. Thus, we may expect that the stationary-point approximation will yield an accurate result, with many stationary points contributing to the sum. Moreover, because the phase varies greatly across the scattering screen, we may assume that the phases ϕ_j, modulo 2π, are uncorrelated and are distributed uniformly in the interval $[0, 2\pi]$.

The electric field for a point on the observing plane, which we take to be $\mathbf{b} = 0$, is given by

$$E(0) \;=\; E_0 \sum \frac{e^{i\phi_j}}{H_j}. \tag{1.21}$$

Because it is the sum of many phasors of random length and phase, the central limit theorem tells us that the components of *E,* assuming that the weights H_j and phases ϕ_j are uncorrelated, are distributed normally, so that

$$P_E(E) \;=\; \frac{1}{\pi I_0} e^{-\frac{|E|^2}{I_0}}, \tag{1.22}$$

where $\sqrt{I_0 / 2}$ is the width of the two-dimensional Gaussian. The observed intensity $I = |E|^2$ therefore follows the exponential distribution,

$$P_I(I) \;=\; \frac{1}{I_0} e^{-\frac{I}{I_0}}. \tag{1.23}$$

Hence, we can identify the constant I_0 with the average observed intensity.

We may furthermore relate I_0 to E_0. The average intensity $\langle I \rangle = I_0$ at a point in the observing plane is given by

$$\langle I \rangle \;=\; \langle E(0) E^*(0) \rangle \;=\; \langle |E_0|^2 \sum_{i,j} \frac{e^{i\phi_i}}{H_i} \frac{e^{-i\phi_j}}{H_j} \rangle, \tag{1.24}$$

where the brackets denote averaging over an ensemble of scattering screen with similar statistics. Because the phase of the stationary points are uncorrelated, only the terms where $i = j$ will survive the ensemble average, so we get

$$\langle I \rangle \;=\; |E_0|^2 \langle \sum_i \frac{1}{H_i^2} \rangle \;=\; \alpha^2 |E_0|^2 \int P(\mathbf{x}) d\mathbf{x} \;=\; \alpha^2 |E_0|^2 \tag{1.25}$$

Here, we evaluated the expectation value of the sum over stationary points using the probability distribution $P(\mathbf{x})$ given in equation (1.20). The constant α is just a normalization constant for the weights. We may absorb this constant into E_0, so that, henceforth, we may write $\langle I \rangle = |E_0|^2$.

1.6.3 Decorrelation Bandwidth

To find the intensity autocorrelation function, we need to know how the intensity varies with frequency. The frequency dependence enters through the phase of the exponentials, and to show this dependence explicitly, we may express the phase in terms of the angular frequency ω and a delay τ_i:

$$\omega\tau_i = \phi_i = k(1/2R + 1/2D)\mathbf{x}_i^2 + \Phi(\mathbf{x}_i). \tag{1.26}$$

The first term in τ_i corresponds to the delay due to the extra distance the ray must travel because it scatters off of the point $\mathbf{x}_i$ instead of traveling through the center of the scattering screen while the second term accounts for the delay due to electron density fluctuations. The first term dominates and essentially determines the delay; however, τ_i still inherits the stochastic characteristics of the screen phase, which eliminates correlations in phase between stationary points.

The decorrelation bandwidth is defined to be the half-width at half-maximum of the intensity autocorrelation function. Using our expression for the intensity, we get

$$\begin{aligned}\langle I(\omega)I(\omega+\Delta\omega)\rangle &= \left\langle |E_0|^2 \sum_{i,j} \frac{e^{i\omega\tau_i}}{H_i}\frac{e^{-i\omega\tau_j}}{H_j} |E_0|^2 \sum_{l,m} \frac{e^{i(\omega+\Delta\omega)\tau_l}}{H_l}\frac{e^{-i(\omega+\Delta\omega)\tau_m}}{H_m} \right\rangle \\ &= \left\langle |E_0|^4 \sum_{i,j,l,m} \frac{e^{i\omega\tau_i}}{H_i}\frac{e^{-i\omega\tau_j}}{H_j}\frac{e^{i\omega\tau_l}}{H_l}\frac{e^{-i\omega\tau_m}}{H_m} e^{i\Delta\omega(\tau_l-\tau_m)} \right\rangle\end{aligned} \tag{1.27}$$

where the brackets denote averaging over an ensemble of scattering screens. Again, because the phases of the stationary points are uncorrelated, only the terms where $i = j$ and $l = m$ or where $i = l$ and $j = m$ survive the ensemble average, and the expression for the autocorrelation function simplifies to

$$\langle I(\omega)I(\omega + \Delta\omega)\rangle = \langle I\rangle^2 + \left\langle |E_0|^4 \sum_{i,j} \frac{1}{H_i^2} \frac{1}{H_j^2} e^{i\Delta\omega(\tau_j - \tau_i)} \right\rangle . \tag{1.28}$$

Using the probability distribution given in equation (1.20) for the distribution of stationary points, we may evaluate the second term explicitly to get

$$\begin{aligned} \frac{\langle I(\omega)I(\omega + \Delta\omega)\rangle}{\langle I\rangle^2} &= 1 + \int e^{i\Delta\omega(\tau_j - \tau_i)} P(\mathbf{x}_i)P(\mathbf{x}_j) d\mathbf{x}_i d\mathbf{x}_j \\ &= 1 + \frac{1}{1 + (\Delta\omega\tau_0)^2} \end{aligned} \tag{1.29}$$

with $\tau_0 = (1/R + 1/D)r_R^2/c$. The decorrelation bandwidth is therefore

$$\Delta\nu_{ISS} = \frac{1}{2\pi\tau_0} = \frac{c}{2\pi} \frac{1}{r_R^2} \frac{RD}{R + D}, \tag{1.30}$$

and from comparing this result to the uncertainty relation, we may identify τ_0 as the temporal broadening.

1.6.4 Visibility in the Observing Plane

In interferometry, observers measure the visibility C_{AB}, the product of the electric fields measured at two stations, A and B, on a baseline $\mathbf{b}$. Using our expression for the electric field for points on the observing plane, we have

$$\begin{aligned} C_{AB}(\mathbf{b}) &= E(A)E^*(B) \\ &= E_0 \sum_i \frac{e^{i\phi_i}}{H_i} E_0^* \sum_j \frac{e^{-i\phi_j}}{H_j} e^{-ik(\mathbf{x}_j \cdot \mathbf{b})/D} \end{aligned} \tag{1.31}$$

The normalized average visibility is therefore

$$\bar{V}(\mathbf{b}) = \frac{1}{\langle I\rangle}\langle C_{AB}(\mathbf{b})\rangle = \frac{1}{\langle I\rangle}\langle |E_0|^2 \sum_i \frac{1}{H_i^2} e^{-ik(\mathbf{x}_i \cdot \mathbf{b})/D} \rangle \quad (1.32)$$

Again, using equation (1.20), we can calculate the expected value, and we find that the normalized average visibility is given by

$$\bar{V}(\mathbf{b}) = \int P(\mathbf{x}) e^{-ik(\mathbf{x} \cdot \mathbf{b})/D} d\mathbf{x} = \exp\left[-\frac{1}{2}(k\theta b)^2\right] \quad (1.33)$$

The average visibility varies on a length scale $1/k\theta$, and this length scale corresponds to the size of the diffraction maxima:

$$b_0 = \frac{1}{k\theta} = \frac{\lambda}{2\pi\theta}. \quad (1.34)$$

Alternatively, we can see how the electric field varies in the observing plane to determine the typical size of the diffraction maxima. As seen in equation (1.19), the dependence of the electric field on baseline **b** enters via the term $ik(\mathbf{x}_j \cdot \mathbf{b})/D$ in the exponent. Since the scattering disk has a characteristic size r_R, coherence in the observing plane occurs on a length scale b_0 where

$$\frac{k r_R b_0}{D} = 1. \quad (1.35)$$

Because $r_R = \theta D$, we find again that $b_0 = \lambda / 2\pi\theta$.

1.6.5 Decorrelation Bandwidth in Interferometry

The autocorrelation function of the visibilities is given by

$$\langle C_{AB}(\omega) C_{AB}{}^*(\omega + \Delta\omega)\rangle = \quad (1.36)$$

$$\langle |E_0|^4 \sum_{i,j,l,m} \frac{e^{i\omega\tau_i}}{H_i} \frac{e^{-i\omega\tau_j}}{H_j} e^{-i\frac{\omega}{c}\frac{\mathbf{x}_j \cdot \mathbf{b}}{D}} \frac{e^{-i(\omega+\Delta\omega)\tau_l}}{H_l} \frac{e^{i(\omega+\Delta\omega)\tau_m}}{H_m} e^{i\frac{(\omega+\Delta\omega)}{c}\frac{\mathbf{x}_m \cdot \mathbf{b}}{D}} \rangle$$

As before, only the terms where $i = j$ and $l = m$ or where $i = l$ and $j = m$ survive the ensemble average, and we get

$$\begin{aligned}\langle C_{AB}(\omega)C_{AB}^*(\omega+\Delta\omega)\rangle &= \langle |E_0|^4 \sum_{i,l} \frac{1}{H_i^2} e^{-i\frac{\omega}{c}\frac{\mathbf{x}_i\cdot\mathbf{b}}{D}} \frac{1}{H_l^2} e^{i\frac{(\omega+\Delta\omega)}{c}\frac{\mathbf{x}_l\cdot\mathbf{b}}{D}} \rangle + \\ &\quad \langle |E_0|^4 \sum_{i,j} \frac{1}{H_i^2}\frac{1}{H_j^2} e^{i\Delta\omega(\tau_j-\tau_i)} e^{i\frac{\Delta\omega}{c}\frac{\mathbf{x}_j\cdot\mathbf{b}}{D}} \rangle\end{aligned} \tag{1.37}$$

We can evaluate the expected values as before. In the first term, the sums decouple, with each sum equal to the expression for the average visibility, albeit evaluated at different frequencies, and in the second term, the term linear in $\mathbf{x}_j$ can be eliminated by a suitable change of variable when evaluating the integral. The end result is

$$\frac{\langle C_{AB}(\omega)C_{AB}^*(\omega+\Delta\omega)\rangle}{\langle I\rangle^2} = \langle \bar{V}(\mathbf{b},\omega)\bar{V}(\mathbf{b},\omega+\Delta\omega)\rangle + \frac{1}{1+(\Delta\omega\tau_0)^2} \tag{1.38}$$

The angular size θ is of order milliarcseconds, so for short baselines, we have $k\theta b \ll 1$ and $\bar{V}(\mathbf{b}) \cong 1$. Not surprisingly, in this limit, we obtain

$$\frac{\langle C_{AB}(\omega)C_{AB}^*(\omega+\Delta\omega)\rangle}{\langle I\rangle^2} \cong 1 + \frac{1}{1+(\Delta\omega\tau_0)^2}, \tag{1.39}$$

an expression identical to the intensity autocorrelation function.

1.6.6 Scintillation Velocity

The scintillation velocity V_{ISS} is defined to be

$$V_{ISS} = \frac{b_0}{t_{ISS}} = \frac{\lambda D}{2\pi r_R t_{ISS}}. \tag{1.40}$$

Using equation (1.30), we can eliminate r_R to get

$$V_{ISS} = \frac{\lambda}{t_{ISS}}\sqrt{\frac{\Delta\nu_{ISS}(R+D)(D/R)}{2\pi c}} = \frac{\sqrt{c\Delta\nu_{ISS}(R+D)(D/R)/2\pi}}{\nu t_{ISS}} \tag{1.41}$$

To express this result in a more traditional form, we define $x \equiv D/R$ and note that $L = D + R$ is the distance to the pulsar. In terms of these quantities, the relation becomes

$$V_{ISS} = \frac{\sqrt{\Delta\nu_{ISS} L x (c/2\pi)}}{\nu t_{ISS}}, \tag{1.42}$$

or in terms of common astrophysical units,

$$V_{ISS} = A_V \frac{\sqrt{\Delta\nu_{ISS,\,\mathrm{MHz}} L_{\mathrm{kpc}} x}}{\nu_{\mathrm{GHz}} t_{ISS}}\ \mathrm{km\ s^{-1}} \tag{1.43}$$

where $A_V = 3.85 \times 10^4$. Gupta, Rickett, & Lyne (1994) obtained an identical result; however, others have derived similar results differing only in the numerical constant A_V, which depends on the exact definitions of $\Delta\nu_{ISS}$ and t_{ISS}. Lyne & Smith (1982), for example, used a value of 2×10^4 while Cordes (1986) and Harrison & Lyne (1993) used a value of 1.27×10^4.

From the scintillation velocity V_{ISS}, one can infer the velocity of the pulsar using a lever-arm argument, as illustrated in Figure 1.4. After a time t, the pulsar, initially at $(\mathbf{0}, R + D)$, will have moved to $(\mathbf{V}_{pm} t, R + D)$, where $\mathbf{V}_{pm}$ is the velocity of the pulsar. Similarly, a point on the screen initially at $(\mathbf{0}, D)$ will have moved to $(\mathbf{V}_S t, D)$, where $\mathbf{V}_S$ is the velocity of the screen, and a point of the interference pattern initially at the origin in the observing plane will have moved to $(\mathbf{V}_{ISS} t, 0)$. Hence, we have

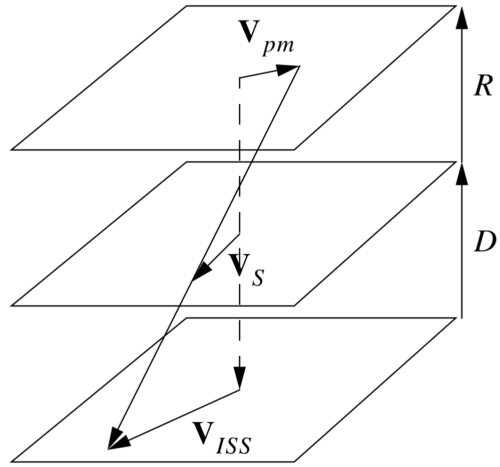

Figure 1.4— Geometry of the lever-arm argument relating the scintillation velocity to the velocities of the pulsar and the screen.

$$(\mathbf{V}_{ISS}t, 0) - (\mathbf{V}_{pm}t, R + D) = \frac{R + D}{R}[(\mathbf{V}_S t, D) - (\mathbf{V}_{pm}t, R + D)]. \quad (1.44)$$

Solving for $\mathbf{V}_{ISS}$ yields

$$\mathbf{V}_{ISS} = (1 + x)\mathbf{V}_S - x\mathbf{V}_{pm} \quad (1.45)$$

where $x = D / R$.

Pulsars generally move with high speed while the interstellar medium moves with low speed; therefore, we have $|\mathbf{V}_s| \ll |\mathbf{V}_{pm}|$ and $V_{ISS} = |\mathbf{V}_{ISS}| \approx x|\mathbf{V}_{pm}|$. When $x = 1$, as usually assumed, the scintillation velocity equals the velocity of the pulsar. Studies by Lyne & Smith, Cordes, and Gupta et al. compared velocities derived from scintillation methods with those measured using other methods and found the two sets of results were correlated. Scintillation methods, however, systematically underestimated the proper motion of pulsars (Harrison & Lyne). Gupta (1995) reexamined the correlation using the revised value of A_V and taking into account revisions to the pulsar distance scale (Taylor & Cordes 1993) and found that the systematic bias disappeared and that the two sets of results agreed quite well statistically.

A discrepancy between V_{ISS} and V_{pm} indicates that the assumption $x = 1$ is violated. In this case, we can infer the distance to the scattering screen. Solving for x gives

$$x \approx \left(A_V \frac{\sqrt{\Delta\nu_{ISS,\,\mathrm{MHz}} L_{\mathrm{kpc}}}}{\nu_{\mathrm{GHz}} t_{ISS} V_{pm,\mathrm{km/s}}} \right)^2, \tag{1.46}$$

and the distance to the screen is given by

$$D = \frac{x}{1 + x} L. \tag{1.47}$$

Chapter 2

Experiment

2.1 Motivation

Of the known pulsars, PSR J0437-4715 has the lowest dispersion measure, $DM = 2.6484\ \mathrm{cm}^{-3}$ pc, providing us with one compelling reason to observe this particular pulsar. Phillips & Clegg (1992) observed B0950+08, the pulsar with the second-lowest dispersion measure known, at 50 MHz and found a decorrelation bandwidth much larger than expected in light of reported results from observations at higher frequencies. Their result moved this pulsar down significantly in the temporal broadening-vs.-dispersion measure plot and showed that it clearly departed from the trend of other low-*DM* pulsars. Previous measurements of the decorrelation bandwidth for PSR J0437-4715 suggest that this pulsar is a typical low-DM pulsar. But these measurements were made at higher frequencies, and we were interested in seeing if PSR J0437-4715 would exhibit behavior similar to PSR B0950+08 at lower frequencies.

PSR J0437-4715, moreover, is the closest known millisecond pulsar. Its strength and proximity, at a distance of 180 pc (Sandhu et al. 1997), make it a good candidate to probe the local ISM, and it also has a well-defined bow shock (Fruchter 1998). The bow shock and the surface of the Local Bubble are two regions which could conceivably dominate the scattering of radiation from this pulsar (Britton 1996).

2.2 Observation

We observed PSR J0437-4715 at two epochs using the Very Long Baseline Array (VLBA) operated by the National Radio Astronomy Observatory (NRAO). For both observations, the 32-MHz bandwidth consisted of four adjacent 8-MHz intermediate-frequency (IF) bands.

On 1996 November 5, we observed the pulsar at a center frequency of 332 MHz over four 33-minute scans, using 25-meter telescopes at Fort Davis (FD), Mauna Kea (MK), Pie Town (PT), and St. Croix (SC). We had a spectral resolution of 250 kHz, splitting the 32-MHz bandwidth across 128 channels. Between scans of the pulsar, we observed extragalactic sources for calibration purposes.

On 1999 April 8, we observed the pulsar for two 44-minute scans and one 33-minute scan, using the telescopes at Fort Davis, Kitt Peak (KP), Los Alamos (LA), Mauna Kea, Owens Valley (OV), Pie Town, and St. Croix. We split the 32-MHz bandwidth, centered at 328 MHz, into 256 channels to achieve a spectral resolution of 125 kHz. To increase the signal-to-noise ratio, the data for this observation were correlated using a gate which covered 12% of the pulse period and which isolated the central peak of the pulse profile.

2.3 Data Calibration

2.3.1 Radio-Frequency Interference

I began the calibration using NRAO's Astronomical Image Processing System (AIPS). The data from both observations were marred by radio-frequency interference (RFI). The second observation in particular suffered badly from RFI, forcing us to eliminate the Kitt Peak and Owens Valley antennas from the outset. The interference also tainted some of the measurements of the system temperature. The system temperature should not change abruptly, so if an isolated reading clearly departed from an otherwise smooth trend, I merely removed that value. In two IFs, however, rampant corruption due to RFI obliterated evidence of a smooth evolution in system temperature. For these two IFs, I copied the system temperatures from an adjacent IF, as system temperatures should not vary wildly from IF to IF.

I examined the remaining visibilities and flagged channels and time ranges to eliminate data corrupted by very strong, narrow-band signals typical of man-made sources. I applied the usual corrections, as described in the *AIPS Cookbook*, for the effects of antenna parallactic angles, digital sampler bias, system temperature, and gain calibration.

2.3.2 Phase Calibration

An interferometer consists of two telescopes on a baseline of length *b*. As illustrated in Figure 2.1, the signal to second telescope must travel an extra distance

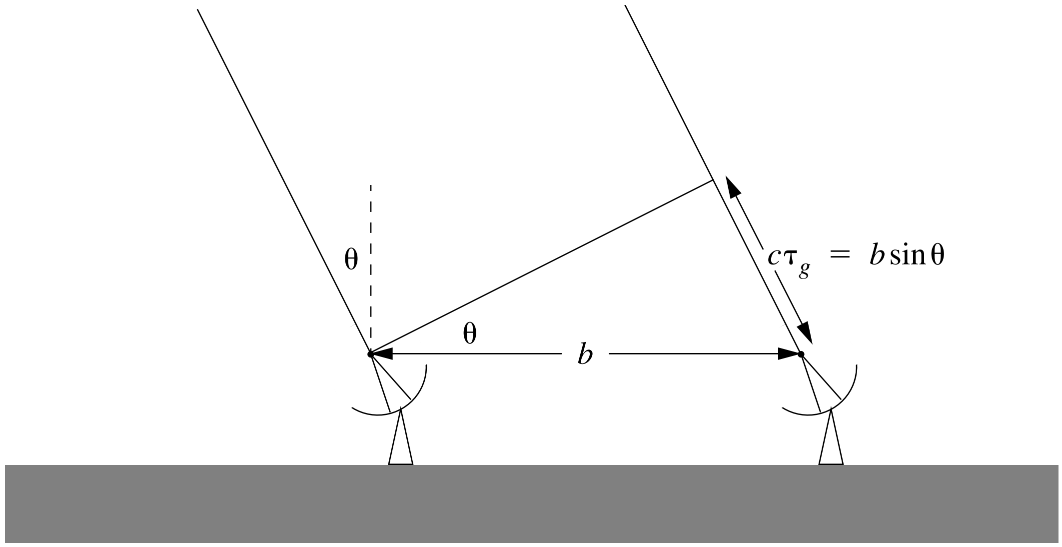

Figure 2.1—The signal must traverse an additional distance $b\sin\theta$ to reach the second antenna and arrives at a time τ_g later. Hence, the signals at the two antennas differ by a phase of $\omega\tau_g$.

$b\sin\theta$ and arrives at that telescope a time $\tau_g = b\sin\theta / c$ later; thus, the phase of the signals at the two telescope differ by $\phi = \omega\tau_g$. The geometric delay τ_g, moreover, varies with time as the Earth rotates and the telescopes track the source. Before multiplying the two signals together, the correlator attempts to synchronize the two signals by introducing an instrumental delay τ_I to compensate for the geometric delay; when the geometric delay and instrumental delay do not perfectly cancel, however, the visibility phase will vary with time and frequency. The residual fringe rate corresponds to the rate at which the phase varies with time, and the residual multiband delay, to the rate at which the phase varies with frequency.

The upper plot in Figure 2.2 shows the average visibility phase obtained from a one-minute interval of calibrator data before I applied any phase calibrations. The

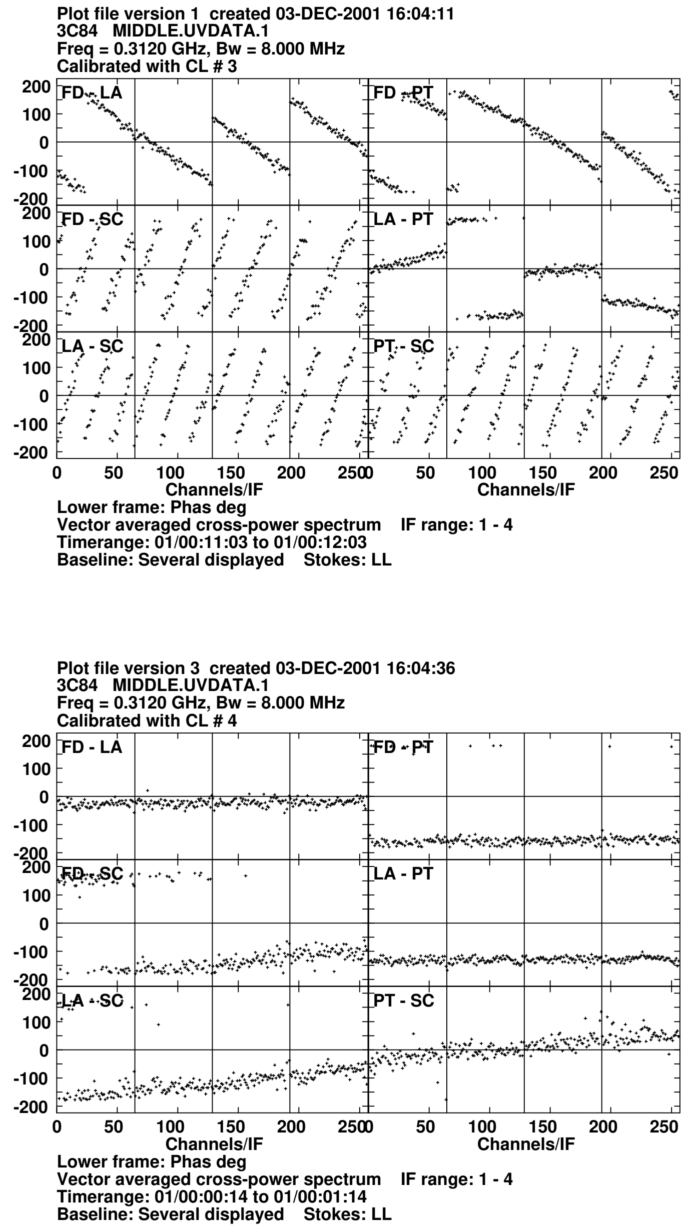

Figure 2.2— The upper plot shows the average visibility phase for a one-minute interval of calibrator data. The phase jumps discontinuously between IFs due to differing electronic delays among the baseband converters, and the residual multiband delay results in the phase slope with frequency. The lower plot shows the average visibility phase for a different one-minute interval of calibrator data after the manual phase calibration. The phase no longer jumps discontinuously between IFs, but it still exhibits the effects of the residual delays and rates.

discontinuities in phase result from single-band delays, the varying electronic delays between IFs, while the slopes within each IF result from the residual multiband delays. Fringing a short interval of calibrator data will determine the electronic delay differences between IFs. The interval has to be long enough to provide a good signal-to-noise ratio but short enough to preserve phase coherence. Fortunately, a one-minute interval readily provided a signal-to-noise ratio of at least ten, easing the task of finding an interval of calibrator data free of RFI on most of the baselines.

The lower plot in Figure 2.2 shows the average visibility phase for a different one-minute interval of calibrator data after application of the single-band-delay solutions. The phase now varies continuously across IFs; however, the variation with frequency reveals the presence of the residual multiband delay, and the overall non-zero level evidences the cumulative effects of the residual fringe rate. To correct the visibility phases for these effects, I ran a fringe fit on each source. After applying those solutions, I wrote the visibilities for the calibrator source 3C84 and for PSR J0437-4715 to separate FITS files on disk. The rest of the calibration was done outside of AIPS.

2.3.3 Bandpass Calibration

With the initial phase calibration complete, I could now average the visibilities over time and perform a bandpass calibration. For each baseline, I averaged the complex visibilities from a ten-minute interval of calibrator data. Deviations from a flat amplitude and phase spectrum reflected the non-ideal frequency response of the baseband converters, an example of which is shown in Figure 2.3. The gain of the filters drops off at the ends of each IF, significantly reducing the signal-to-noise ratio in the first and last channel of each IF. These channels, furthermore, are the least likely to satisfy closure relationships. Consequently, I omitted these channels in the subsequent analysis. I then smoothed the data using boxcar averaging with a one-minute window to further increase the signal-to-noise ratio.

2.3.4 Scattering by the Ionosphere and Solar Wind

At this point, I had applied all the standard calibration procedures for VLBI data; however, our low observing frequency introduced complications that required additional corrections. As shown in Figure 2.4, the visibility phase after fringe fitting exhibited significant curvature with frequency because of the dependence of excess path length on frequency. The fringe fits remove the constant and linear dependence of the phase on observing frequency, but it does not remove higher-order terms. The longer baselines exhibit more phase curvature than do shorter baselines because

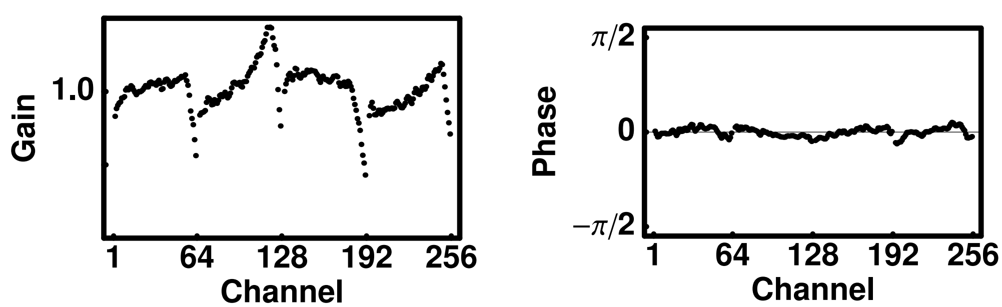

Figure 2.3— The gain and phase response of the baseband converters on the Fort Davis-Pie Town baseline.

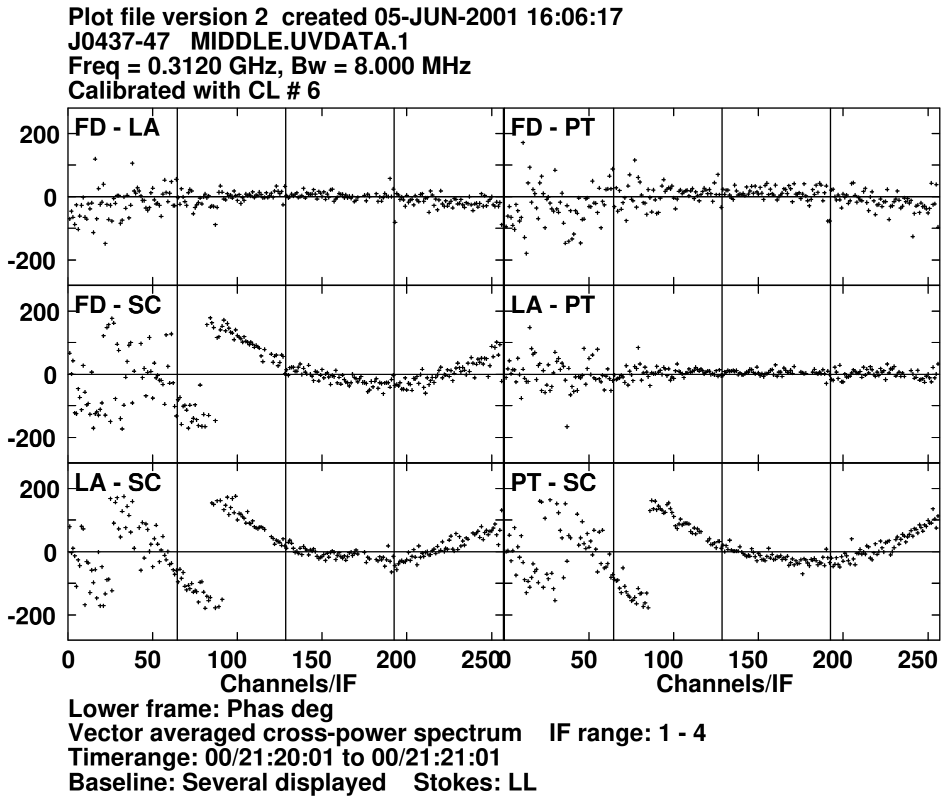

Figure 2.4— The visibility phase plotted as a function of frequency after the residual fringe rate and residual delay have been removed. Propagation through the ionosphere causes the observed curvature in phase.

differences in the lines of sight increase with baseline length.

The electron density in the ionosphere corresponds to a plasma frequency ν_p of order 10 MHz, which is much less than our observing frequency; hence, the excess path length in the zenith direction is approximately

$$L_0(\nu) = \int_0^{\infty} [n(\nu, h) - 1] dh \cong -\frac{40.3}{\nu^2} \int_0^{\infty} N(h) dh \text{ m} \tag{2.1}$$

where $n(\nu, h)$ is the index of refraction, $N(h)$ is the electron distribution in m^{-3}, h is height, and ν is the frequency in Hz. Expanding about $\nu = \nu_0$ gives

$$L_0(\nu_0 + \Delta\nu) \;=\; L_0(\nu_0)\left(1 + \frac{\Delta\nu}{\nu_0}\right)^{-2} \cong L_0(\nu_0)\left[1 - 2\left(\frac{\Delta\nu}{\nu_0}\right) + 3\left(\frac{\Delta\nu}{\nu_0}\right)^2\right] \tag{2.2}$$

With $\Delta\nu\,/\,\nu_0 \cong 0.1$ and a total electron content of $10^{16} \sim 10^{17}\ \mathrm{m}^{-2}$, the quadratic term corresponds to a path length of $0.1 \sim 1.1$ m, which is of the same order as our observing wavelength.

In an attempt to correct the visibility phases, I calculated amplitude-weighted phase averages for each channel and then fit the results to a quadratic polynomial. I then used this polynomial to find the appropriate phase to subtract from each frequency channel. Although this recipe removed much of the quadratic dependence, it did not remove it entirely. Plots of the average visibility phase still exhibited some curvature, and the phase of the autocorrelation functions still exhibited a linear dependence with frequency lag, indicating a lingering quadratic dependence in the data.

In his doctoral dissertation, Britton described broadband phase variations in his data and attributed these variations to weak scattering by the ionosphere and solar wind. Acoustic-gravity waves in the upper atmosphere cause large-scale variations in electron density of 0.5% to 5% on time scales of ten to twenty minutes (Thompson, Moran, & Swenson 1986), and at an observing frequency of 330 MHz, these disturbances can easily result in phase variations on the order of one radian. Similarly, irregularities in the solar wind will weakly scatter radiation, resulting in broadband phase fluctuations, albeit on a shorter time scale of order one minute.

Our data exhibited the same broadband variations. Figure 2.5 shows examples

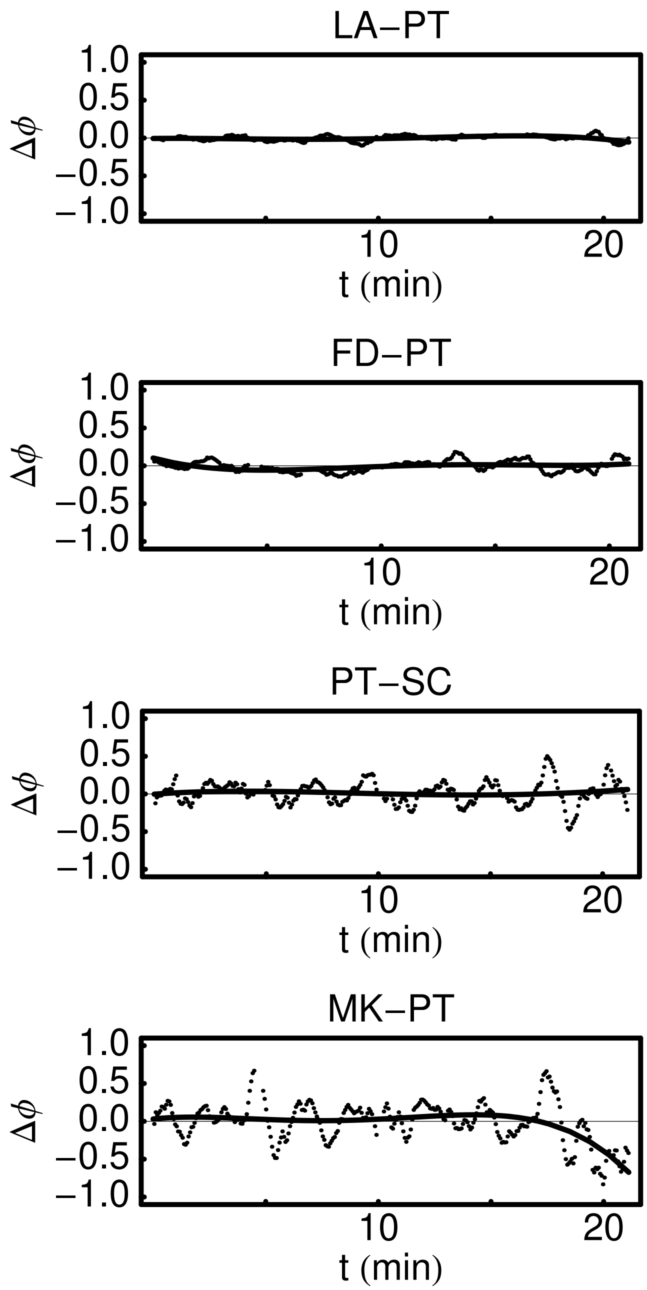

Figure 2.5— Broadband phase variations occur on a time scale of about one minute, and the amplitude of the variation increases with baseline length, indicating the variations are caused by weak scattering in the solar wind.

of these variations for several baselines. The fluctuations occur on two time scales. The longer time scale of about fifteen minutes corresponds to weak scattering in the ionosphere; the fluctuations on the short time scale of about one minute grow in amplitude with baseline length, characteristic of scattering by the solar wind. The plots also show the best-fitting eighth-order polynomial, which I used to remove from the data the time-dependent phase variations due to the ionosphere.

Removing these variations reduced the amount of spread in the average visibility phase of each frequency channel, leading to better fits in the procedure to eliminate the phase curvature. Figure 2.6 shows an example of how effectively the procedure removed the quadratic term.

To verify that my calibration procedure did not introduce any unintended biases, I calculated two-dimensional autocorrelation functions for each data set for the calibrator source. As expected, I obtained results flat in both time and frequency lags, except for a spike at small time and frequency lags due to the effects of noise.

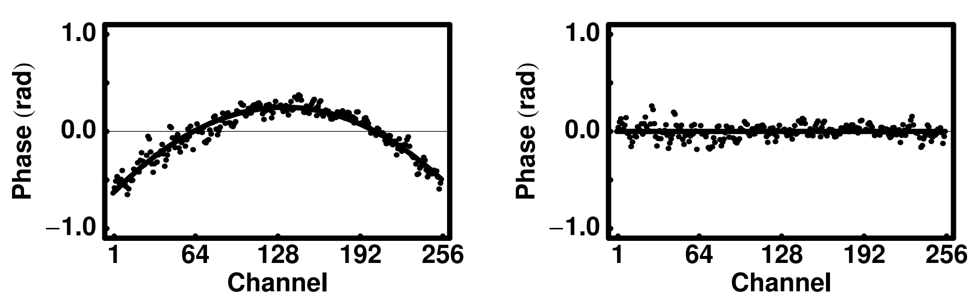

Figure 2.6— The visibility phase has a quadratic dependence on frequency, as shown in the left plot, due to propagation through the ionosphere. After using the best-fitting parabola to estimate and remove this term, the visibility phase averages to zero.

2.4 Data Analysis

Initially, we had hoped to measure the angular broadening of the pulsar by measuring the phase variations of the diffraction pattern; however, several complications derailed our efforts. Most significant, the decorrelation bandwidth was much larger than expected–close to the total observing bandwidth. As the phase variations of the diffraction pattern have this characteristic bandwidth (Desai 1992), they could not be distinguished from ionospheric phase, phase slope, and curvature. Furthermore, we did not obtain fringes on the longest baseline where we expect phase variations of the diffraction pattern to be largest.

The remaining baselines were of comparable lengths, so I chose to focus on the Fort Davis-Pie Town baseline. Figure 2.7 shows plots of the visibility amplitudes for the pulsar on this baseline for both epochs. The white vertical lines correspond to the channels omitted at the ends of each IF, and the white horizontal lines correspond to breaks in the scan or to time ranges flagged because of RFI. At both epochs, we detected scintillation maxima that typically persist for ten to twenty minutes and that span several IFs, suggesting a characteristic width in frequency on the order of ten megahertz.

To determine the decorrelation bandwidth, I calculated the two-dimensional autocorrelation functions for the Fort Davis-Pie Town baseline. Figure 2.8 shows the amplitude of one such autocorrelation function, with the noise spike removed. The contours divide the range of the function into ten equally sized intervals. I fit the

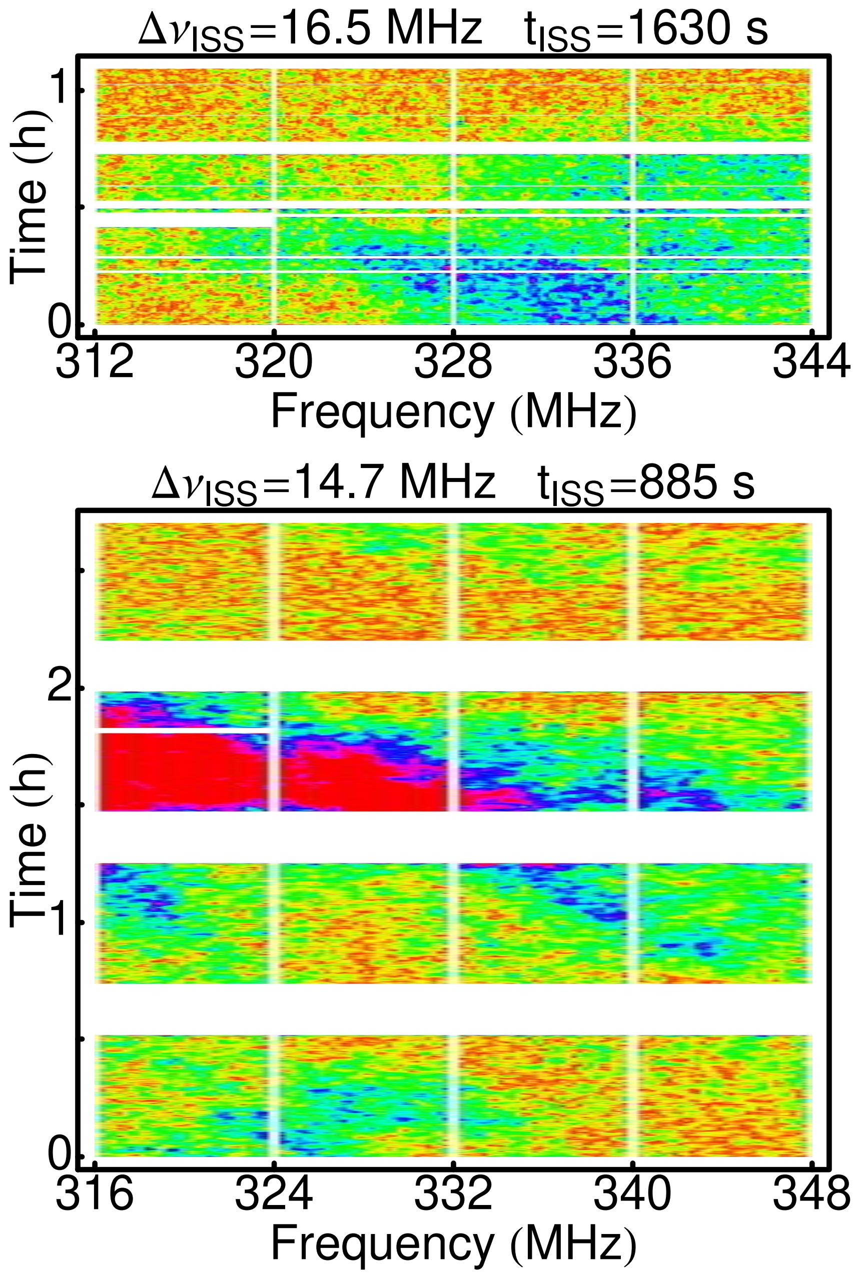

Figure 2.7— These plots show the visibility amplitude as a function of frequency and time for observations of PSR J0437-4715 on the Fort Davis-Pie Town baseline on 1996 November 5 (*bottom*) and 1999 April 8 (*top*). The scintillation maxima typically span several IFs and persist for ten to twenty minutes.

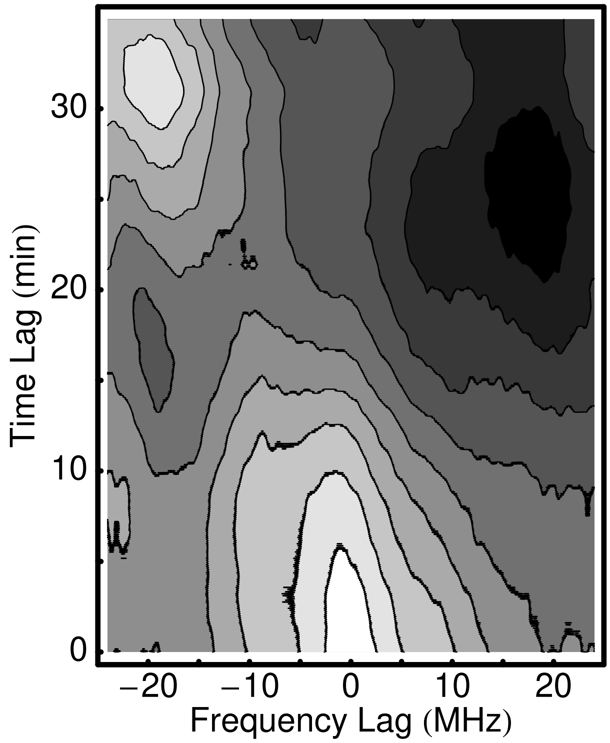

Figure 2.8— A contour plot of the two-dimensional autocorrelation function amplitude obtained for the Fort Davis-Pie Town baseline. The characteristic width along the time-lag axis is the decorrelation bandwidth, and the characteristic width along the frequency-lag axis is the scintillation time scale.

frequency-lag axis of the two autocorrelation functions to the form given in equation (1.39). To each point used in the fit, I assigned a weight equal to the square root of the number of pairs used to calculate that point. The fits yielded a decorrelation bandwidth of 14.7 $\pm$ 0.5 MHz for the first epoch and 16.5 $\pm$ 0.5 MHz for the second. The uncertainties represent the 95%-confidence level of the fits.

Neither epoch individually produced a correlation function with a form particularly close to the predicted theoretical form; however, the composite autocorrelation function obtained by suitably combining the two individual functions

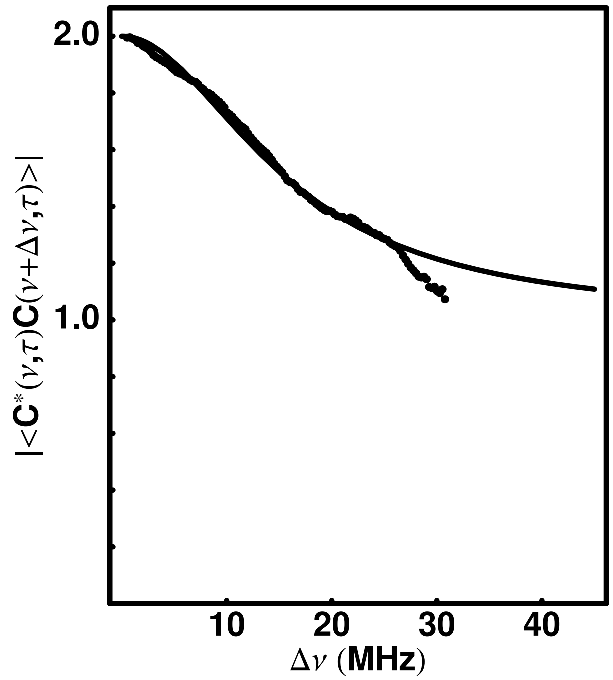

Figure 2.9— The composite autocorrelation function obtained by suitably combining the autocorrelation functions from the two observations. The best-fitting Lorentzian has a characteristic width of $\Delta\nu_{ISS} = 15.7 \pm 0.2$ MHz.

did. To combine the two functions, I first halved the spectral resolution of the second-epoch function by averaging two adjacent bins, weighted according to the number of contributing pairs, into one bin, and then I averaged the two autocorrelation functions together bin by bin, again assigning weights proportional to the number of pairs contributing to a bin. The resulting function, shown in Figure 2.9, matched the theoretical prediction well. The solid line shows the best-fit results, from which we obtained a decorrelation bandwidth of 15.7 ± 0.2 MHz. Again, the uncertainty represents a 95%-confidence level.

To estimate the scintillation time scale, I fit the correlation function along the

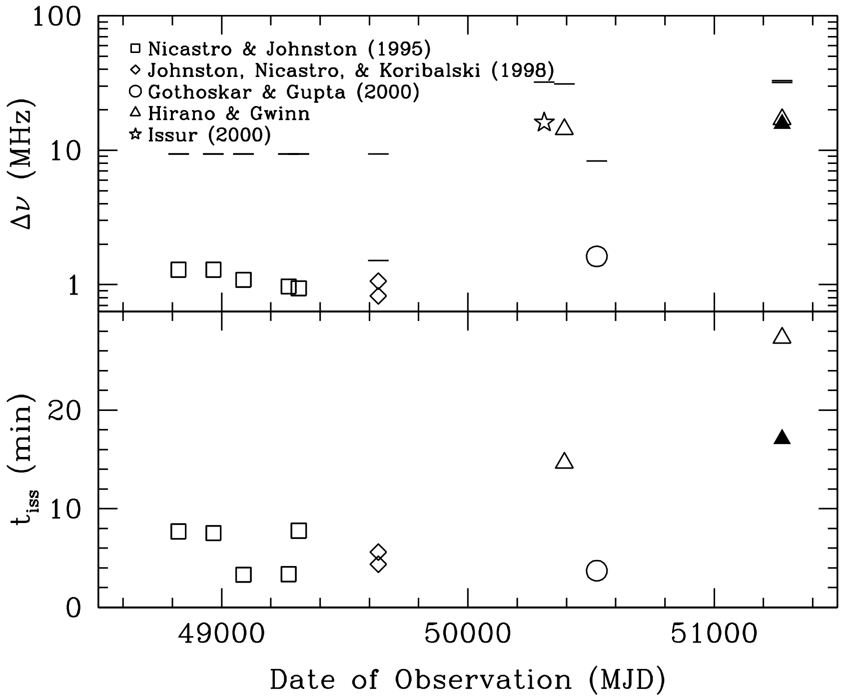

Figure 2.10—Measurements of the decorrelation bandwidth and scintillation time scale plotted against observing date. The horizontal lines indicate the effective bandwidth used for each measurement. The solid triangles show our estimates of $\Delta\nu_{ISS}$ and t_{ISS} derived from the composite autocorrelation function. All of our estimates lie outside of the bandwidth used in most of the previous observations.

time-lag axis to the function $A + Be^{-\Delta t^2 / t_{ISS}^2}$. The parameters of the fit were the offset A and the amplitude B and width t_{ISS} of the Gaussian. The fits yielded estimates for t_{ISS} of 885 $\pm$ 9 s for the first epoch, 1630 $\pm$ 80 s for the second, and 1020 $\pm$ 70 s for the composite autocorrelation function.

2.5 Results

2.5.1 Scintillation Bandwidth

Figure 2.10 shows measurements of the decorrelation bandwidth $\Delta\nu_{ISS}$ and scintillation time scale t_{ISS} for PSR J0437-4715, rescaled to an observing frequency of 330 MHz. The horizontal lines indicate the equivalent observing bandwidth for each measurement. Our estimates of $\Delta\nu_{ISS}$ agree with a decorrelation bandwidth of 0.5 ± 0.1 MHz at 150 MHz obtained by Issur (2000), but they clearly do not agree with the other estimates. Our estimates of the scintillation time scale are also inconsistent with earlier measurements.

One possible explanation for the discrepancy is that the nature of the scattering changes significantly with time. Bhat (1999) observed that scintillation parameters often vary with time. Pulsars generally move with high speeds and therefore the line of sight to a pulsar may pass through regions of widely varying electron density on relatively short time scales. Rays from distant pulsars must still travel through many density fluctuations; consequently, any effect due to the pulsar's motion will tend to average out. However, the proximity of nearby pulsars like PSR J0437-4715 reduces the number of independent regions so that one might expect to see the scintillation parameters change significantly with time.

Observations of PSR J0437-4715 arguably do not support the hypothesis that the scattering parameters change by an order of magnitude on a regular basis. Gothoskar & Gupta (2000) found a decorrelation bandwidth of 1.56 MHz at an observing frequency of 327 MHz, consistent with the earlier results, from data taken 130 days after our first observation. Such a significant change over this time period would suggest that the scattering occurs in a small region close to the pulsar, yet Nicastro & Johnston (1995) observed PSR J0437-4715 at 436 MHz at five epochs over a 488-day period and did not see a dramatic shift in the decorrelation bandwidth.

A more intriguing possibility is that we are measuring different parameters than those in the earlier observations. The effective bandwidth of earlier observations corresponds to the width of one of our IFs, and as seen in Figure 2.10, our points lie outside this bandwidth because, as seen in Figure 2.7, a scintillation maximum typically spans several IFs. If the decorrelation bandwidth scales as expected with observing frequency, the earlier experiments may have detected evidence of structure within an intensity maximum that covered the entire observing bandwidth.

VLBI observations have an advantage over single-dish observations in these cases. In interferometry, because the noise is independent for each antenna, the average visibility will vanish when the signal vanishes; hence, we can easily tell whether or not the scintillation intensity goes to zero even when an intensity maximum regularly encompasses nearly the entire bandwidth. In single-dish experiments, the receiver noise must be manually separated from the signal, allowing for the possibility that part of the signal is misidentified as noise.

2.5.2 Fine-Scale Structure within Scintillation Maxima

Figure 2.11 shows an expanded view of a scintillation maximum. The amplitude varies with a modulation index of approximately 0.2, and the variations appear to occur with a characteristic bandwidth of order 1 MHz and on a time scale of a few minutes. Interestingly, these figures would agree with the estimates of the scintillation bandwidth and time scale from the earlier observations.

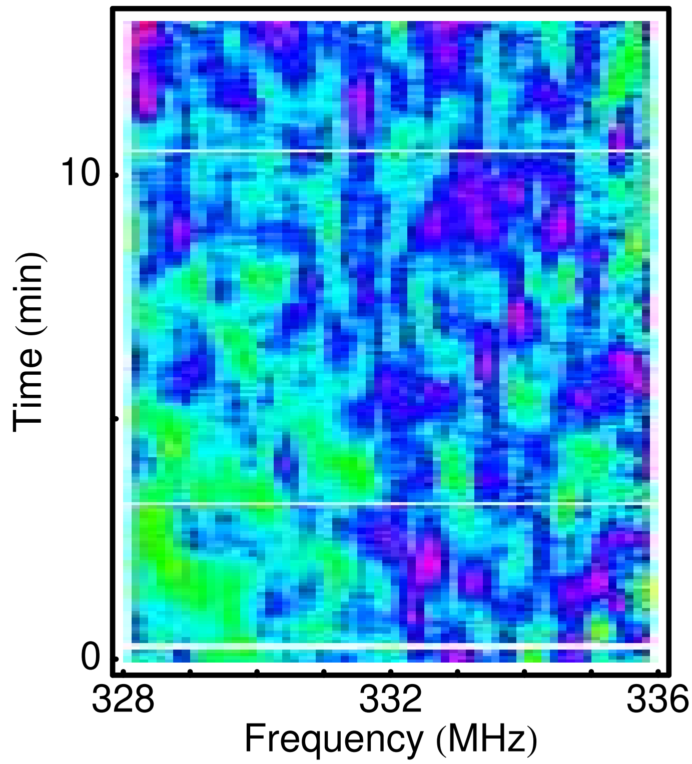

Figure 2.11—Variations in the visibility amplitude within a scintillation maximum appear to occur over a frequency scale on the order of 1 MHz.

To extract evidence of a second characteristic scale, I focused on the most prominent intensity maximum from each observation, treating the two subsets of data individually. In both cases, I did not apply Hanning smoothing to the data to avoid obscuring evidence of the smaller scale. The component of the visibility due to the large scale modulation overwhelms the component responsible for the small scale modulation, in calculations of the autocorrelation function, so I subtracted off the average visibility first in an attempt to uncover any small-scale correlations.

The two resulting autocorrelation functions, one of which is shown in the

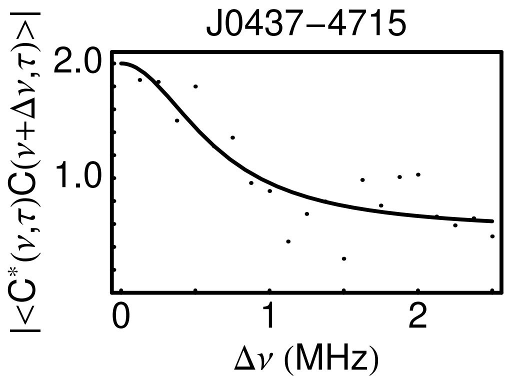

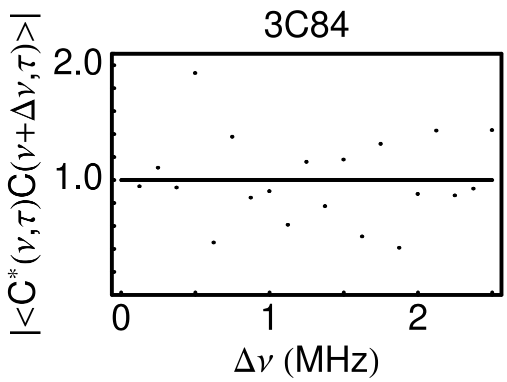

Figure 2.12—An autocorrelation function calculated for a portion of the pulsar (*upper*) data reveals correlations for small frequency lags of order 0.6 MHz. The autocorrelation function for calibrator source 3C84 (*lower*), in contrast, exhibits no correlations.

upper plot in Figure 2.12, revealed correlations on scales of 0.6 MHz and 0.4 MHz. To verify that these results were not an artifact of the procedure, I applied the same procedure to data from the calibrator source. The result, shown in the lower plot, exhibits no evidence of correlation. In both plots, the spike due to noise at zero lag has been removed.

The time-averaging required to increase the signal-to-noise ratio unfortunately smears the noise spike in the autocorrelation function, obscuring some

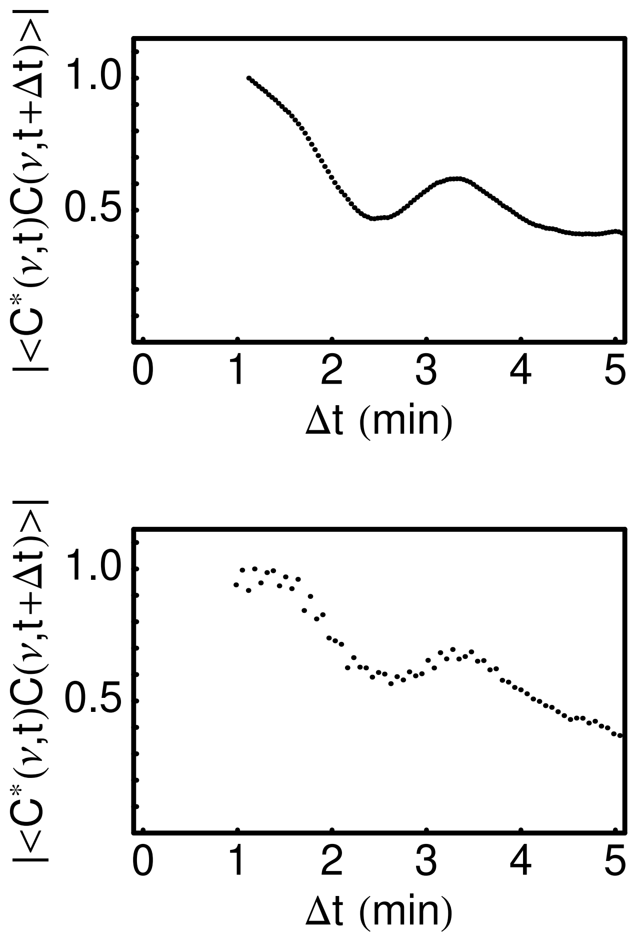

Figure 2.13—The time-domain autocorrelation functions for the maxima from the first (*upper*) and second (*lower*) epochs reveal correlation on a time scale of one to two minutes.

evidence of correlation for small time lags. The upper plot in Figure 2.13 reveals correlations for small time lags on the order of one to two minutes for the first-epoch maximum. The autocorrelation function calculated for the other epoch from the un-Hanning-smoothed data did not show any evidence of correlation; however, using smoothed data revealed correlations at small time lags, again on the order of one to two minutes, as seen in the lower plot.

These results agree roughly with the earlier measurements of the scintillation bandwidth and time scale, but they tend toward smaller values. The measurements at 436 MHz and 660 MHz by Johnston, Nicastro, & Koribalski (1998) scale respectively to 1.1 MHz and 0.82 MHz at 330 MHz, and Gothoskar & Gupta found a decorrelation bandwidth of 1.56 MHz at an observing frequency of 327 MHz. Their reported values for t_{ISS}, appropriately rescaled, range from three to eight minutes, except for one value at just under two minutes.

Internal structure may arise if the scattering has more than one characteristic decorrelation bandwidth as is the case for the Crab pulsar. Scattering of this pulsar by its supernova remnant and by the ISM along the line of sight produces two characteristic pulse broadening times (Lyne & Thorne 1975, Isaacman & Rankin 1977). PSR J0437-4715 could exhibit similar behavior; scattering may occur, for instance, at its bow shock and at the surface of the Local Bubble.

The small characteristic bandwidth, however, seems to conflict with the small modulation index. On the one hand, the small bandwidth indicates that the phase changes rapidly with frequency. The scattering deflects rays through angles large enough to cause significant differences in optical path length for small changes in frequency. For a change in frequency of order the characteristic bandwidth then, the phase differences should result in completely destructive interference so that the modulation index should be of order unity. On the other hand, a small modulation index typically arises because the phase changes slowly with frequency, limiting the variations in amplitude. Significant fluctuations in amplitude therefore occur only over large changes in frequency. A scattering mechanism consistent with our data must cause rapid changes in phase yet keep these changes bounded. It would be a precarious balancing act.

Instead, the fine structure may arise due to interference between multiple images in the observing plane. Cordes & Wolszczan (1986) and recently Stinebring et al. (2001), for example, have shown that multiple imaging of pulsars accounts for secondary features, such as multiple drift slopes, in pulsar dynamic spectra, and Gupta, Bhat, and Rao (1999) have even analyzed these secondary features for PSR B1133+16 to infer the size of the pulsar's emission region. Taking the Fourier transform of the autocorrelation function reveals telltale attributes of this phenomenon; however, an analysis of our data did not uncover these attributes, probably due to a low signal-to-noise ratio. Alternatively, the fine structure we see may be the result of a different mechanism altogether, a possibility we are currently exploring.

2.5.3 Temporal Broadening of Nearby Pulsars

The estimate of the decorrelation bandwidth corresponds to a broadening time of $\tau_s = 5.0\times10^{-11}$ s at 1 GHz. (Because τ_s is less than the wave period at 1 GHz, τ_s should be viewed simply as a parameter and not the actual pulse broadening observable at that frequency.) As seen in Figure 2.14, the relatively large decorrelation bandwidth, corresponding to a small estimate of the broadening time, moves PSR J0437-4715, despite its small dispersion measure, significantly toward the

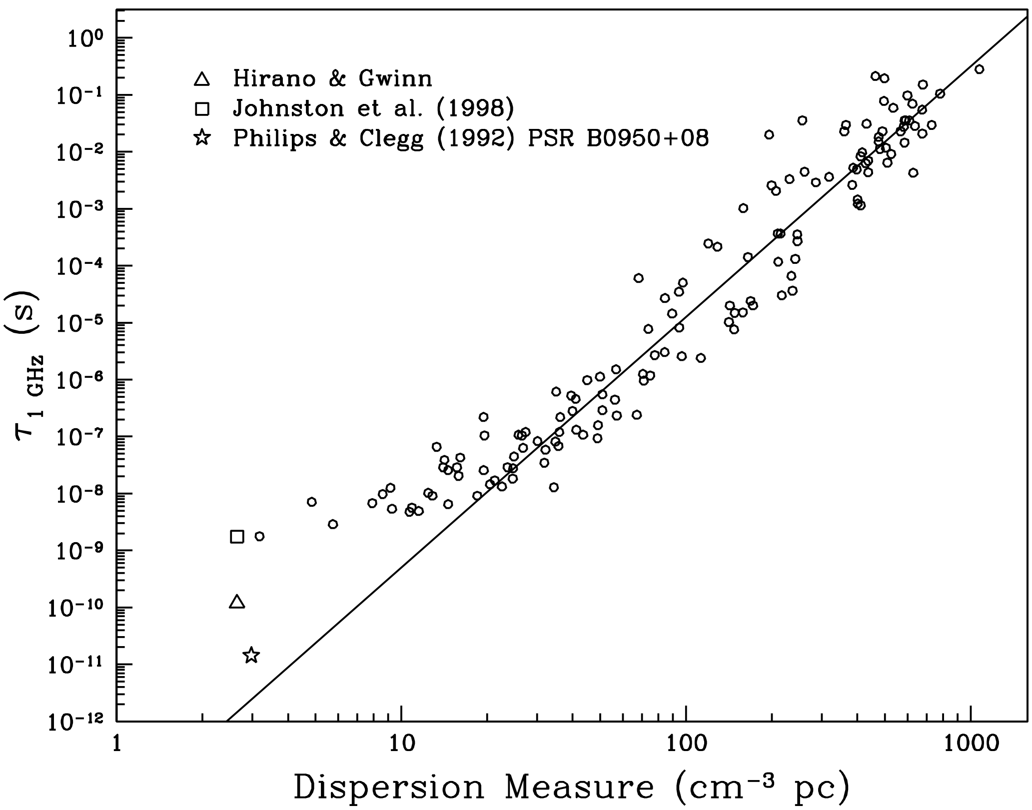

Figure 2.14—The plot of temporal broadening vs. dispersion measure with the location of PSR J0437-4715 revised with our estimate of the temporal broadening. Our upward revision of the decorrelation bandwidth moves PSR J0437-4715 down significantly toward the trend extrapolated from high-*DM* pulsars. Low-frequency observations of B0950+08 resulted in a similar revision for its location on the diagram.

trend followed by pulsars with large dispersion measures; the previous estimates, in contrast, suggest that the pulsar behaves like a typical low-*DM* pulsar.

PSR B0950+08, which has a dispersion measure of 2.9702 cm^{-3} pc, similarly follows the trend of pulsars with large dispersion measures. Observing at 47 MHz and 51 MHz, Phillips & Clegg also found a decorrelation bandwidth much larger than expected and attributed underestimates of the decorrelation bandwidth at higher frequencies to insufficient observing bandwidth.

These two cases suggest that other pulsars, particularly those with low dispersion measures, may have temporal broadening significantly smaller than represented in the literature. For both PSR B0950+08 and PSR J0437-4715, observations at lower frequencies and wider bandwidth resulted in sharp upward revisions of the decorrelation bandwidth, leading to sharp downward revisions of the inferred temporal broadening τ_s. For PSR B0950+08, earlier observations had reported intensity variations with frequency and time that varied greatly between observing epochs and often did not resemble that expected from scintillation (Armstrong & Rickett 1981, Roberts & Ables 1982, Cordes et al. 1985, Smirnova & Shabanova 1992). Phillips & Clegg, with observations at 50 MHz, showed that these variations were much narrower in bandwidth and shorter in time scale than the actual scintillations. Similarly, for PSR J0437-4715, observations at higher frequencies and narrower bandwidth may have misinterpreted fine structure within the diffraction pattern as scintillations, resulting in underestimates of the scintillation parameters.

Sutton, who first noted the elbow in Figure 2.14, recognized that the temporal broadening of the two pulsar populations were determined using different methods. For high-*DM* pulsars, temporal broadening is measured directly by examining the pulse shape while for low-*DM* pulsars, it is inferred from the decorrelation bandwidth. Stinebring et al. find that fine structure in the scintillation pattern occurs commonly among nearby pulsars. Misidentification of fine structure as the fundamental scintillation pattern could be common among such pulsars and could move at least some of the pulsars at *DM* of 30 cm^{-3} pc or less in Figure 2.14 to lower τ_s, providing an instrumental explanation for the "kink" in that figure, rather than Sutton's more traditional explanation in terms of scattering by HII regions.

2.5.4 Measure of Turbulence in the Local ISM

I estimated the parameter C_n^2 in equation (1.10) using the relation

$$C_n^2 = 2\times10^{-6}\nu_{\mathrm{MHz}}^{11/3}D_{\mathrm{pc}}^{-11/6}\Delta\nu_{\mathrm{kHz}}^{-5/6}\ \mathrm{m}^{-20/3} \tag{2.1}$$

where ν_{MHz} is the observing frequency in megahertz, D_{pc} is the pulsar distance in parsecs, and $\Delta\nu_{\mathrm{kHz}}$ is the decorrelation bandwidth in kilohertz (Rickett). For PSR B0950+08, Phillips & Clegg found values of $\log C_n^2$ ranging from -4.4 to -4.7 and noted that these values were significantly smaller than estimates obtained for other nearby pulsars, where the least scattered pulsars had values of $\log C_n^2$ close to -3.5.

For PSR J0437-4715, I find $\log C_n^2 = -4.1$, a value which is higher than for PSR B0950+08 but lower than those for the other nearby pulsars. Because our observing bandwidth is only twice the decorrelation bandwidth, we may be underestimating the true decorrelation bandwidth; a larger decorrelation bandwidth would further lower our estimate of C_n^2, bring it closer to the values found for PSR B0950+08.

2.5.5 Scintillation Velocity

The scintillation velocity should equal the proper motion velocity if the scattering screen is located midway between the observer and source. Using equation (1.42) with $x = 1$ and $L = 180$ pc, I obtained a scintillation velocity of

$V_{ISS} = 192$ km s^{-1}, which agrees with previous measurements of the scintillation velocity. Johnston et al. obtained a value of 170 km s^{-1} from observations at 436 MHz, and Gothoskar & Gupta measured a mean scintillation velocity of 231 km s^{-1} from observations at 327 MHz. Proper motion measurements, however, have yielded significantly lower results. Bell et al. (1995) found a velocity of 91 ± 3 km s^{-1}, and Toscano et al. (1999), using arrival-time methods, recently obtained a velocity measurement of 120.5 ± 0.2 km s^{-1}. This disparity suggests that the assumption that scattering screen lies midway between the observer and source is not valid for PSR J0437-4715.

I used equation (1.46) with $V_{pm} = 120.5$ km s^{-1} and equation (1.47) to infer the distance to the scattering screen and found that the scattering material is located at a distance of 129 pc. Gothoskar & Gupta estimate that the shell of the Local Bubble lies at a distance of 120 pc along this line of sight; hence, I identify the scattering screen with the shell of the Local Bubble. Gothoskar & Gupta reached the same conclusion from their data.

Chapter 3

Published Papers

A Ray-Tracing Model of the Vela Pulsar

C. Hirano and C. R. Gwinn
Department of Physics, University of California, Santa Barbara, CA 93106

Published in *The Astrophysical Journal*, 553:358–366, 2001 May 20.

ABSTRACT

In the relativistic plasma surrounding a pulsar, a subluminal ordinary-mode electromagnetic wave will propagate along a magnetic field line. After some distance, it can break free of the field line and escape the magnetosphere to reach an observer. We describe a simple model of pulsar radio emission based on this scenario and find that applying this model to the case of the Vela pulsar reproduces qualitative characteristics of the observed Vela pulse profile.

INTRODUCTION

Soon after the discovery of pulsars, Goldreich & Julian (1969) deduced the basic structure of the magnetosphere. The strong corotating magnetic field of order 10^8–10^{12} G dominates the physics in the surrounding region. The rotating magnetic field produces forces sufficient to rip electrons from the stellar surface with high energy. The high-energy electrons emit photons which in turn quickly decay via pair production. This process repeats until the energies fall sufficiently to halt pair production. The consequent corotating charge distribution cancels the $\mathbf{v} \times \mathbf{B}$ forces, except perhaps at certain gaps, and the intense magnetic field constrains the particles to move along the field lines. The end result is a one-dimensional relativistic electron-positron wind flowing out along the corotating magnetic field lines. Those particles on the field lines which extend beyond the light cylinder can escape to infinity.

Connecting this theoretical picture with observation has proven to be difficult; we still do not understand the physical mechanism which generates pulsar radio emissions. Observations of pulsars reveal that the individual pulses from a pulsar vary greatly from pulse to pulse with no apparent pattern. Averaging several hundred pulses, however, yields a stable profile characteristic of a pulsar, yet these characteristic profiles still differ widely from pulsar to pulsar (Lyne & Graham-Smith 1998). Rankin (1983) has proposed that pulsars exhibit two distinct types of emissions, core and conal, suggesting that more than one emission mechanism may be at work.

Despite the large variety of integrated pulse profiles, the profiles commonly exhibit a high degree of linear polarization. The polarization position angle often sweeps smoothly through a range of angles of up to 180° (Lyne & Graham-Smith 1998). In their rotating-vector model, Radhakrishnan & Cooke (1969) hypothesized that the radiation was polarized along or orthogonal to the magnetic field lines; the position angle therefore reflects the geometry of a dipolar magnetic field.

While some pulsars exhibit an abrupt jump between orthogonal modes of polarization, their position angle distributions indicate that the emissions contain two components, each of which appear consistent with the rotating-vector model (Manchester 1975; Backer, Rankin, & Campbell 1976). Fluctuations in the flux densities of the two modes would be observed as a sudden jump in position angle (McKinnon & Stinebring 1998).

The pulse also typically broadens with decreasing frequency, a behavior usually attributed to radius-to-frequency mapping: lower-frequency emissions are thought to originate farther away from the stellar surface than higher-frequency emissions (see Cordes (1978) and references therein). Because the magnetic field lines diverge, the higher altitude translates to an increase in the size of the emission region which in turn translates to a wider observed pulse at lower frequency.

Barnard & Arons (1986) investigated the propagation of electromagnetic waves in the relativistic plasma permeating the pulsar magnetosphere and found that one mode, the subluminal O-mode, follows paths along the magnetic field lines. A possible source of this radiation is the pair-production front, where the primary particles decay into those which make up the outflowing plasma (Lerche 1970; Melrose 1996). Lyutikov (1998) has also suggested that cyclotron instabilities in the plasma will produce subluminal O-mode radiation in the magnetosphere of a pulsar.

Observations of rays originating in this mode would reflect the geometry of the dipolar field (Gallant 1996), which could account for some observed pulse shapes and position angle sweeps. In this paper, we consider a model that assumes a neutron star with a corotating dipolar magnetic field and a source of radio-frequency radiation near the stellar surface. By determining the path of rays from the stellar surface to the observer, we attempt to reproduce the pulse intensity and polarization profiles of a pulsar, specifically the Vela pulsar.

WAVE PROPAGATION IN THE PULSAR MAGNETOSPHERE

In a relativistic plasma and a strong magnetic field **B**, electromagnetic waves propagate in two independent, linearly polarized modes. The electric field of an ordinary mode or O-mode wave lies in the (**k**, **B**)-plane, where **k** is the wave vector of the wave; the electric field of the extraordinary mode or X-mode points along the normal to this plane. Because the charges can move only along the field lines, the plasma has no effect on the X-mode, so this mode propagates as if in a vacuum.

In the limit of an infinitely strong magnetic field, the dispersion relation for an O-mode wave of frequency ω propagating in a cold plasma with plasma frequency ω_p and consisting of electrons and positrons moving with speed β_p is given by

$$(\omega^2 - k_{\|}^2)\left\{1 - \frac{\omega_p^2}{\gamma_p^3\omega^2[1 - \beta_p(k_{\|}/\omega)]^2}\right\} - k_{\perp}^2 = 0 \qquad (1)$$

where γ_p is the usual relativistic factor and $k_{\perp}$ and $k_{\|}$ are respectively the components of the wave vector normal to and along the magnetic field (Arons & Barnard 1986). Figure 1 shows a plot of the dispersion relation in the rest frame of the plasma for various values of $k_{\perp}' / \omega_p'$. Here the primes denote quantities measured in the rest

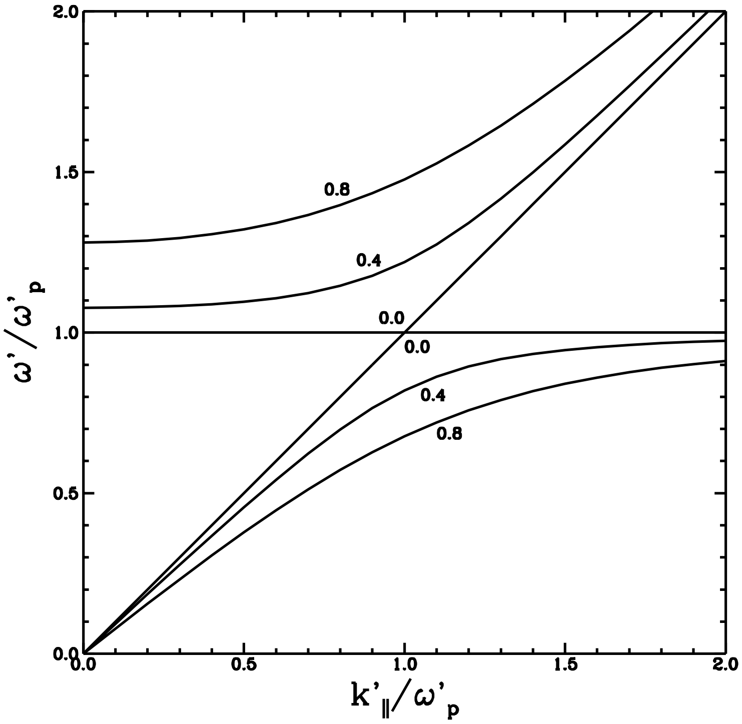

Figure 1.—Plot of the cold plasma O-mode dispersion relation in the rest frame of the plasma for various values of $k_{\perp}' / \omega_p'$, as indicated by the numbers labeling each curve. The upper branch corresponds to the superluminal or fast mode; the lower branch, to the subluminal or slow mode.

frame of the plasma. For each value of $k_{\perp}' / \omega_p'$, the figure shows two curves; the upper branch corresponds to the superluminal or fast mode while the lower branch corresponds to the subluminal or slow mode.

Each ray begins its journey as a slow-mode wave and either transitions to the fast mode and escapes the magnetosphere or succumbs to Landau damping and dissipates in the plasma. We assume the transition occurs via some mechanism, when it reaches a point such that the distance between a pair of curves is minimized, or in other words, when the two types of waves are most alike. We approximate this criterion by requiring the transition to occur when $k_{\|}' / \omega_p' = 1$.

Several points should be made here. First, the criterion which determines where the ray escapes from the magnetosphere will obviously affect the observed pulse shape. The purpose of this paper, however, is not to explore the physics of the mode conversion but rather to examine how refractive effects coupled with the geometry of the dipole field might give rise to features of the pulse profile. Second, the transition criterion we chose corresponds to mode conversion in the weak-turbulence limit (Lyutikov 1998). Turbulence, in effect, smears out the dispersion curves, and the transition occurs via the region in which the smeared curves overlap. Third, the conversion rate may be so low in absolute terms so that it could not account for the observed radio emission. Clearly, the physics of the mode conversion is critical for a complete understanding pulsar radio emission and has been investigated (see, for example, Beskin, Gurevich & Istomin (1988)). However, such a discussion is beyond the intended scope of this paper.

We must also consider that the subluminal mode may interact with the electrons and positrons and transfer its energy to the plasma. The mode conversion can not occur if Landau damping dissipates the wave before it can reach its would-be transition point, but Arons & Barnard (1986) found that for canonical pulsar parameters, Landau damping would not be significant if the mode conversion occurred at radii less than 1000 km. We find that the transition points lie at altitudes significantly less than 1000 km and therefore neglect Landau damping.

In terms of $\omega_p'^2 = \omega_p^2 / \gamma_p$ and $\omega' = \gamma_p(\omega - \beta_p k_{\|})$, where again the primes denote quantities measured in the rest frame of the plasma, the dispersion relation becomes

$$(\omega^2 - k_{\|}^2)\left(1 - \frac{\omega_p{'}^2}{\omega'^2}\right) - k_{\perp}^2 \ = \ 0. \tag{2}$$

It follows that for the subluminal mode because $\omega' < \omega_p{'}$, we must have $|\omega| < |k_{\|}|$. In the corotating frame, the plasma is essentially moving at the speed of light and outruns the wave; boosting to the rest frame of the plasma therefore yields a negative frequency. Consequently, the relevant branch of the dispersion relation is given by

$$\omega' \ = \ -\sqrt{\frac{\omega_p{'}^2 + k_{\|}{'}^2 + k_{\perp}{'}^2 - \sqrt{(\omega_p{'}^2 + k_{\|}{'}^2 + k_{\perp}{'}^2)^2 - 4\omega_p{'}^2 k_{\|}{'}^2}}{2}}. \tag{3}$$

To determine how the wave evolves, we must know how $k_{\perp}{'}$ and $\omega_p{'}$ change as the wave travels away from the stellar surface.

The slow O-mode wave packets obey the relations (Barnard & Arons 1986)

$$\begin{aligned} \frac{r}{r_0} \ &= \ \left(\frac{\theta}{\theta_0}\right)^2 \\ n_{\perp} \equiv \frac{k_{\perp}}{\omega} \ &= \ \frac{3\theta_0}{8}\left(\frac{r}{r_0}\right)^{1/2} - \left(\frac{3\theta_0}{8} - n_{\perp_0}\right)\left(\frac{r}{r_0}\right)^{-3/2} \end{aligned} \tag{4}$$

where r and θ are the spherical coordinates of the wave packet in the corotating frame, with the dipole axis pointing along the z-axis, as illustrated in Figure 2. Here, the 0 subscript denotes values at the stellar surface. The first equation simply says that the wave packet follows the magnetic field lines. The second equation describes how the direction of the wave vector relative to the field line evolves as the wave packet moves along the field line. As the wave moves farther away from the neutron star, the

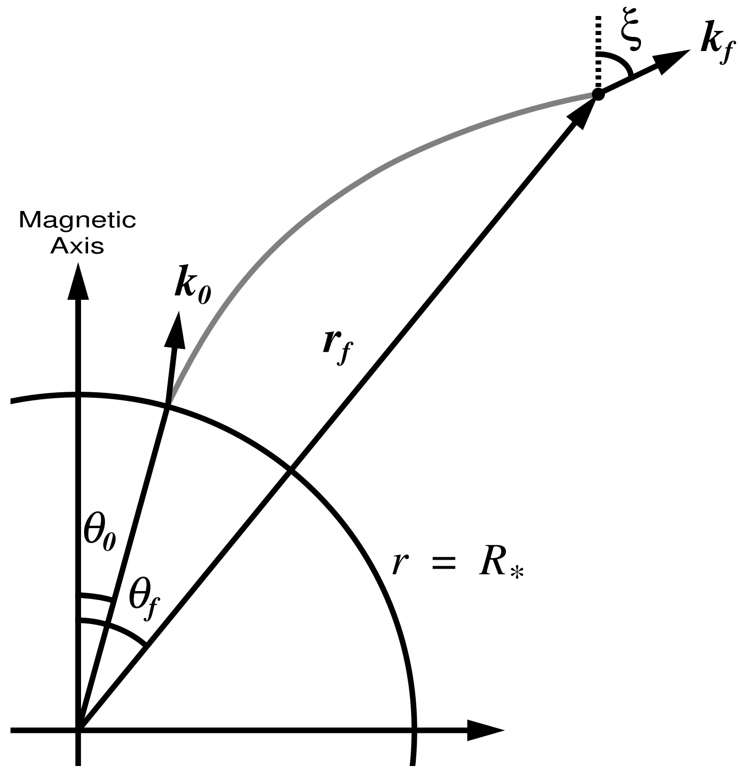

Figure 2.—As shown by the halftone line, the slow-mode wave leaves the stellar surface at (R_*, θ_0) and follows a magnetic field line. At (r_f, θ_f), it transitions to the fast mode and travels along $\mathbf{k}_f$.

orientation of the wave vector depends less on its initial orientation and increasingly on its displacement from the star.

The strong magnetic field constrains the electrons and positrons to move along the field lines; hence, their density is proportional to the magnetic field strength which, for a dipolar magnetic field, varies as r^{-3}. In the corotating frame then, the plasma frequency is given by

$$\omega_p^2(r) = 2\frac{4\pi N_0 e^2}{m}\left(\frac{r_0}{r}\right)^3 \tag{5}$$

where N_0 is the plasma density at $r = r_0$, e is the elementary charge, and m is the mass of the electron. The factor of two reflects the fact that the plasma consists of positrons and electrons. Transforming to the comoving frame introduces a factor of $1 / \gamma_p$ because of length contraction, giving

$$\omega_p'^2(r) = \frac{8\pi N_0 e^2}{\gamma_p m}\left(\frac{r_0}{r}\right)^3 = \omega_{p_0}'^2\left(\frac{r_0}{r}\right)^3 \tag{6}$$

where $\omega_{p_0}' = \omega_p'(r_0)$. In reality, the magnetosphere may contain regions where ω_p does not scale in this manner, and refraction may occur into these regions. Our model neglects this possibility.

Knowledge of both $k_\perp'$ and ω_p' at each point on the trajectory allows us to determine which dispersion relation curve the wave satisfies but not the specific values of ω' and $k_\parallel'$. To find these quantities, we note that the wave also satisfies the Lorentz transformation

$$\omega = \gamma_p(\omega' + \beta_p k_\parallel') \tag{7}$$

where ω is constant in the geometric-optics limit. Plotted on the same axes as the dispersion relation, this relation corresponds to a line with slope $-\beta_p$ and intercept $\omega / \gamma_p \omega_p'$. The intersection of this line with the dispersion relation curve gives us the values of ω' and $k_\parallel'$ for the slow-mode wave at a given radius. Figure 3 shows four pairs of curves, corresponding to distances of ten, twenty, thirty, and forty stellar radii, for a ray following a field line. The dashed curve shows how ω' and $k_\parallel'$ evolve as the ray travels away from the stellar surface.

To find the transition point, we expand equation (3) in powers of $k_\perp' / \omega_p'$

with $k_\parallel' / \omega_p' = 1$ to find

$$\frac{\omega'}{\omega_p'} \approx -1 + \frac{1}{2}\frac{k_\perp'}{\omega_p'} = -1 + \frac{3}{16}\frac{\omega}{\omega_{p_0}'}\theta_0\left(\frac{r}{r_0}\right)^2 \tag{8}$$

Similarly, from equation (7), we have

$$\frac{\omega'}{\omega_p'} = -\beta_p + \frac{\omega}{\gamma_p \omega_p'} = -\beta_p + \frac{\omega}{\gamma_p \omega_{p_0}'}\left(\frac{r}{r_0}\right)^{3/2} \tag{9}$$

Setting these two expressions equal to each other gives

$$1 - \beta_p + \frac{\omega}{\gamma_p \omega_{p_0}'}\left(\frac{r}{r_0}\right)^{3/2} - \frac{3}{16}\frac{\omega}{\omega_{p_0}'}\theta_0\left(\frac{r}{r_0}\right)^2 = 0 \tag{10}$$

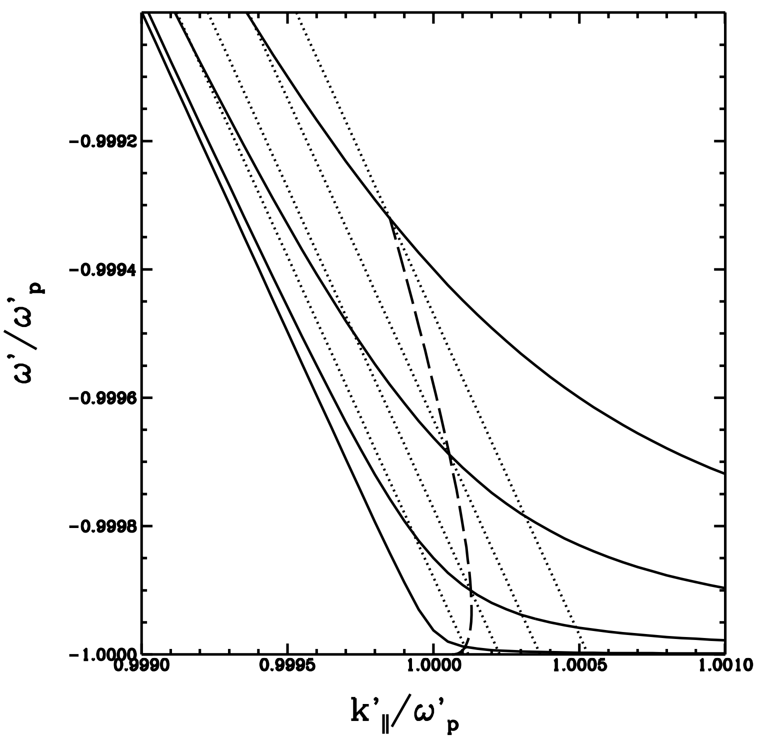

Figure 3.—A line and a dispersion relation curve are associated with each point in the trajectory of an O-mode wave packet. The intersection of the two yields the waves values of ω' and $k_\parallel'$ at that point. The dashed line shows how ω' and $k_\parallel'$ evolve as the wave propagates away from the pulsar.

which may be solved numerically for r / r_0.

After the mode conversion, a ray escapes the magnetosphere as a vacuum electromagnetic wave. The angle between the wave vector and the field line is approximately $n_\perp \approx (3/8)\theta$, and the angle between the field line and the dipole axis is $(3/2)\theta$. Therefore, after the transition occurs, the wave travels along a line that makes an angle $\xi \approx (9/8)\theta_f$ with the axis of the dipolar field, where θ_f is the value of θ at the mode transition.

We simplistically assume in our model that the direction of the wave vector and the polarization remain unchanged by the mode conversion. If the two modes couple due to turbulence within the plasma, one would not expect such a conversion mechanism to preserve **k** and the polarization. Clearly, even in this simple model, the direction of the wave vector must change during the transition; because the phase velocities of the two modes are different, the constraints on ω and $k_\perp$ require that the two modes must have different values of $k_\parallel$. The exact manner in which the slow mode maps to the fast mode depends on details of the conversion process, a discussion of which is beyond the scope of this paper.

RAY TRAJECTORIES

To analyze the path of a wave in the magnetosphere, it is convenient to focus on two reference frames: the observer's frame and the corotating frame. Figure 4 illustrates the relationship between Cartesian coordinates in the two frames. The set denoted by capital letters corresponds to the observer's frame. The *Z*-axis points

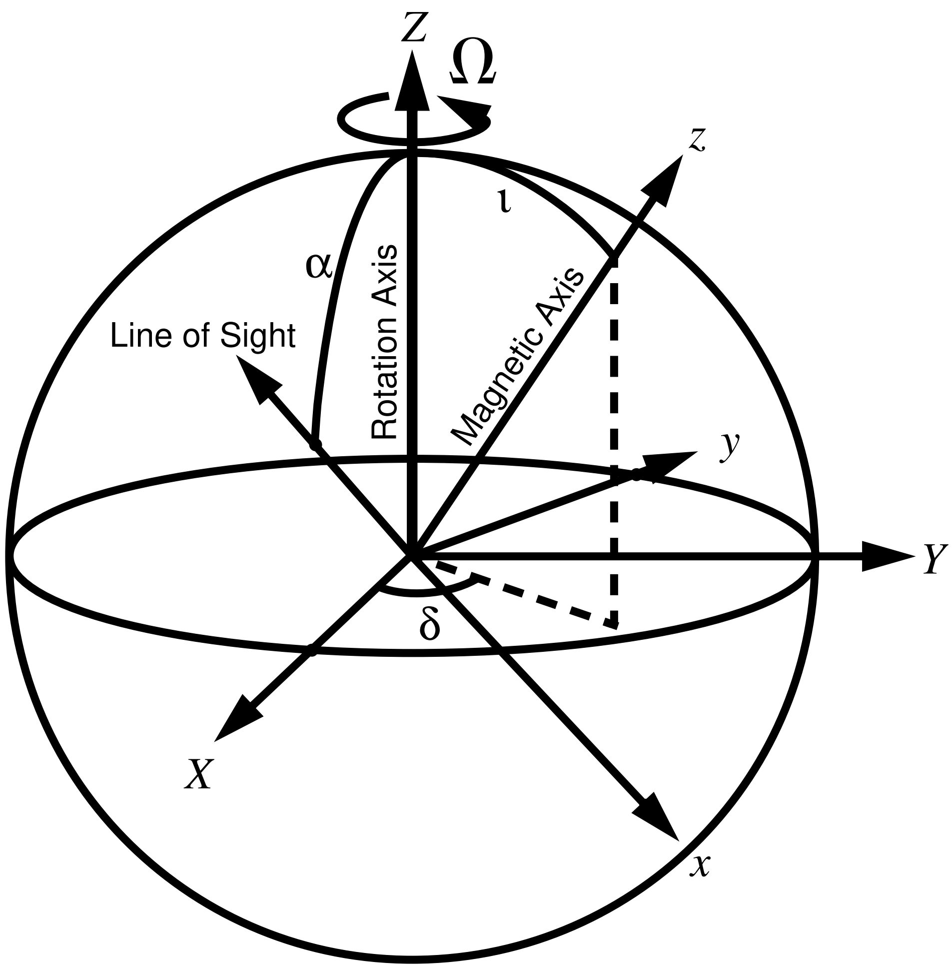

Figure 4.—The axis of rotation points along the Z-axis. The line of sight lies in the XZ-plane and makes an angle α with the rotation axis, and the direction of the magnetic axis is given by the polar angle ι and the azimuthal angle $\delta = \Omega t$.

along the rotation axis of the pulsar, and the line of sight lies in the XZ-plane. The second set, denoted by lower-case variables, lives in the corotating frame. It is related to the first set by a rotation by ι about the Y-axis followed by a rotation by δ about the Z-axis, where the angles δ and ι describe the orientation of the pulsar. In this system, the magnetic axis coincides with z-axis, and the rotation axis lies in the xz-plane.

Finally, because we are working with a dipolar field, the corresponding set of spherical coordinates (r, θ, ϕ) in the corotating frame is useful.

The transition from slow to fast mode may occur at a distance which is a significant fraction of the light cylinder radius; consequently, we must take into account the effects of the boost from the comoving frame to the observer's frame on the wave vector of the ray. The boost changes both the frequency and the direction of the ray. The frequency shift is small, about 1%, and is relatively unimportant. The change in direction, on the other hand, is more significant since the final direction of the ray in the observer's frame determines if and when the ray will reach the observer.

Each point on the transition surface appears to emit a beam of light with a fixed direction in the corotating frame. In the observer's frame, the beams rotate with the star. If a beam makes an angle α with the rotation axis, it will sweep across the line of sight when the star has rotated to an appropriate orientation, and the beam will reach the observer.

Figure 5 illustrates the paths taken by several of these rays as seen from the corotating frame. Up to the transition point, the rays follow the magnetic field lines; after the transition, they travel in the directions given by their wave vectors. In the observer's frame, the rays will travel in straight lines after the transition. In the corotating frame, they will follow spiral trajectories.

CONSTRUCTING THE PULSE PROFILE

To construct the pulse profile, we start with a uniform distribution of rays on the stellar surface centered on the magnetic pole, trace their paths, and select only the ones which will reach the observer. The pulse period is divided into some number of equally-sized bins, and the time of arrival of a ray determines into which bin it goes. Averaging the position angles of the rays contributing to a bin yields the final position

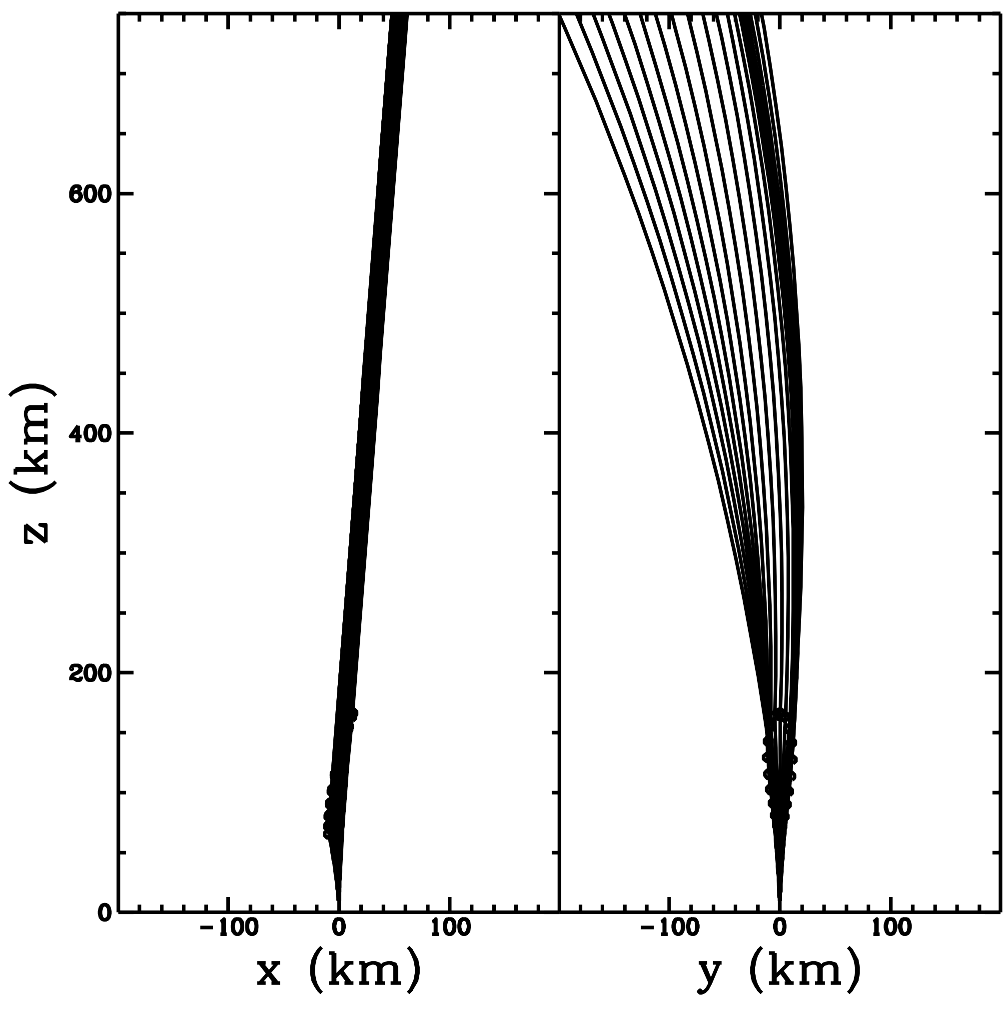

Figure 5.—These figures show the paths of several rays, as seen in the corotating frame, projected onto the *xz*- and *yz*-planes.

angle for that bin.

Each ray carries a Gaussian weighting, with the distribution centered on $\theta_0 = 0$. The width σ_θ of the Gaussian corresponds physically to the size of the beam rising from the stellar surface. Appealing to the central limit theorem, we used a Gaussian distribution so that the resulting profile is not that of a single pulse but that of many averaged together. In other words, the model produces the integrated pulse profile.

For a particular orientation of the neutron star, namely $\delta = 0$, we calculate for each ray its wave vector **K** in the frame of the observer (see Appendix). The time of arrival for a ray that will reach the observer is then given by

$$t_{arr} = -\frac{\phi_K}{\Omega} - \frac{\mathbf{R} \cdot \hat{\mathbf{K}}}{c} \tag{11}$$

where ϕ_K is the azimuthal angle of the wave vector, Ω is the rotational speed of the pulsar, **R** is the point where the ray breaks free of the magnetic field line, and $\hat{\mathbf{K}}$ is the unit vector in the direction of the wave vector. The first term accounts for the fact that the star must rotate to the proper orientation for the ray to align with the line of sight. The second term arises from the displacement of the transition point from the star, as illustrated in Figure 6. The travel time for the light ray from a pulsar at a distance D is approximately $t = D / c$; the actual travel time differs from this value because the wave decouples from the plasma at a displacement **R** from the center of the star.

As mentioned earlier, the rotating-vector model plausibly accounts for the characteristic sweep in position angle under the assumption that the polarization reflects the geometry of the dipolar field. The refraction model of wave propagation naturally explains the alignment of the electric field with the field lines because, for both the O-mode and X-mode, the direction of the electric field is determined by the directions of the magnetic field and the wave vector **k**.

For a dipolar field, the rotating-vector model predicts that the position angle ψ will vary according to

$$\tan\psi(\delta) = \frac{\sin\alpha\sin\delta}{\sin\iota\cos\alpha - \cos\iota\sin\alpha\cos\delta} \tag{12}$$

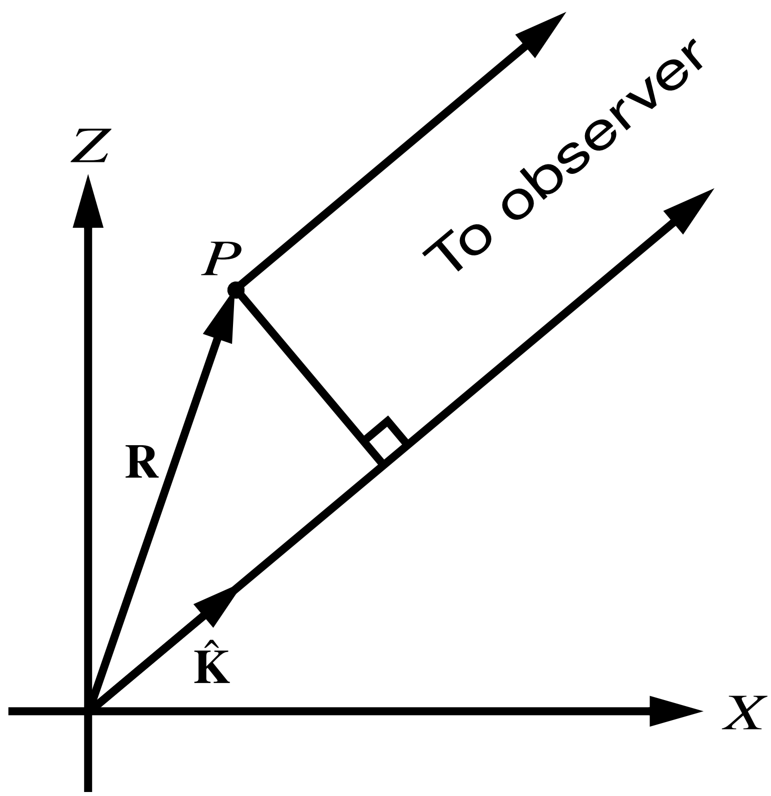

Figure 6.—The ray leaving from point P travels a distance $\mathbf{R}\cdot\hat{\mathbf{K}}$ less than a ray from the origin. Hence, it will arrive at the observer a time $\delta t = \mathbf{R}\cdot\hat{\mathbf{K}}/c$ earlier.

where $\delta = \Omega t$. This relation, however, neglects relativistic and time-of-arrival effects. The transformation from the corotating frame to the observer's frame changes the direction of **E**. Moreover, because of the second contribution to the time-of-arrival delay, a ray corresponding to an orientation δ_1 can arrive before, at the same time as, or after a ray corresponding to $\delta_2 > \delta_1$. These effects may help explain the deviations from the predictions of the basic rotating-vector model that Krishnamohan & Downs (1983) observed with the Vela pulsar.

We obtain the polarization of a ray in the observer frame by calculating the electromagnetic field tensor $F_{\mu\nu}$ for the wave in the corotating frame and then transforming it to the observer frame (see Appendix). To find the electric and magnetic field components in the corotating frame, we define a set of Cartesian coordinate axes so that the z-axis points along the wave vector and the x-axis lies in the (**k**, **B**)-plane. The electric field then points along rotated x-axis, and the magnetic field, along the y-axis.

We have assumed that the electric field of a ray lies in the plane of the dipole field line. Cheng & Ruderman (1979) found that a narrow cone of rays emitted about a field line with initially no average polarization will eventually become nearly completely polarized and that the electric fields will lie in the plane of the dipole field line, if the cone and the direction of the magnetic field become sufficiently misaligned. For radiation due to longitudinal acceleration parallel to **B**, the opening half angle of the cone is of order $\gamma_p^{-1} \approx 0.01$ rad. The angle between the cone and the field line at the transition point is of order $\theta_f \approx 0.1$ rad; hence, our assumption seems reasonable.

RESULTS FROM APPLYING THE MODEL TO THE VELA PULSAR

Our model has eight parameters. Six of these describe the pulsar: R_* is its radial size; T_*, its rotation period; L_*, its spin-down luminosity; ι, the angle between the magnetic field axis and the rotation axis; γ_p, the bulk relativistic factor of the electron-positron wind; and σ_θ, the width of the beam. The two remaining parameters α, the angle between the rotation axis and the line of sight, and ω, the observing frequency, describe the observer.

All of the parameters are set by observations, theory, or the observer except for α, ι, σ_θ, and γ_p. However, observations of polarization often determine the quantity $\alpha - \iota$, and sometimes determine ι as well. Thus, our model contains, in effect, two or three parameters that can be set to change the pulse shape.

The degree to which refractive effects dominate the propagation of the electromagnetic waves depends mainly upon the plasma density on the open field lines. We calculated this density by assuming that the spin-down luminosity of the pulsar is carried away by the electrons and positrons on the open field lines; thus, the ratio L_* / γ_p sets the density of the electron-positron wind at a given radius. We chose to apply the model to the case of the Vela pulsar because its relatively high spin-down luminosity $L_* = 6.918 \times 10^{36}$ erg s^{-1} and correspondingly dense plasma should emphasize the refractive effects.

Vela's short 89.30 ms rotation period translates to a light-cylinder radius of

4236 km. We found that the transitions from slow-mode to fast-mode waves occur within 10% of this distance. Relativistic effects, small as they are, could still have a significant effect on the pulse shape.

We set ι to 90° and R_* to 10 km and chose the values for the remaining parameters $\gamma_p = 100$, $\sigma_\theta = 0.020$ rad, and $\alpha = 94.8°$ so that the model would produce a reasonable pulse shape for an observing frequency of 2.3 GHz. We did not perform an extensive search of the parameter space to study the effects on the pulse profile.

Figure 5 depicts the paths of several rays to the observer as seen in the corotating frame. In this frame, observers follow paths which encircle the magnetic pole and see a pulse when they cut across the "spray" of light. From this figure, we also see that observers would measure the size of the pulsar, i.e. the size of the transition surface, to be around 100 km at 2.3 GHz, a result which agrees reasonably well with recent size measurements of Vela. Macquart et al. (1999) obtained an upper limit of 50 km from 660-MHz scintillation data and suggested that the size of the emission region increases with frequency; Gwinn et al. (2000) measured the size of Vela's emission region to be 440 km; and Krishnamohan & Downs (1983) found a spread in altitude of about 400 km.

Figure 7 shows the intensity profiles obtained from the model for two frequencies and the associated transition surfaces. The dotted curves correspond to 1.4 GHz, and the solid curve, to 2.3 GHz. The larger transition surface at 1.4 GHz results in a wider pulse. A plot of the position angle shows a smooth sweep,

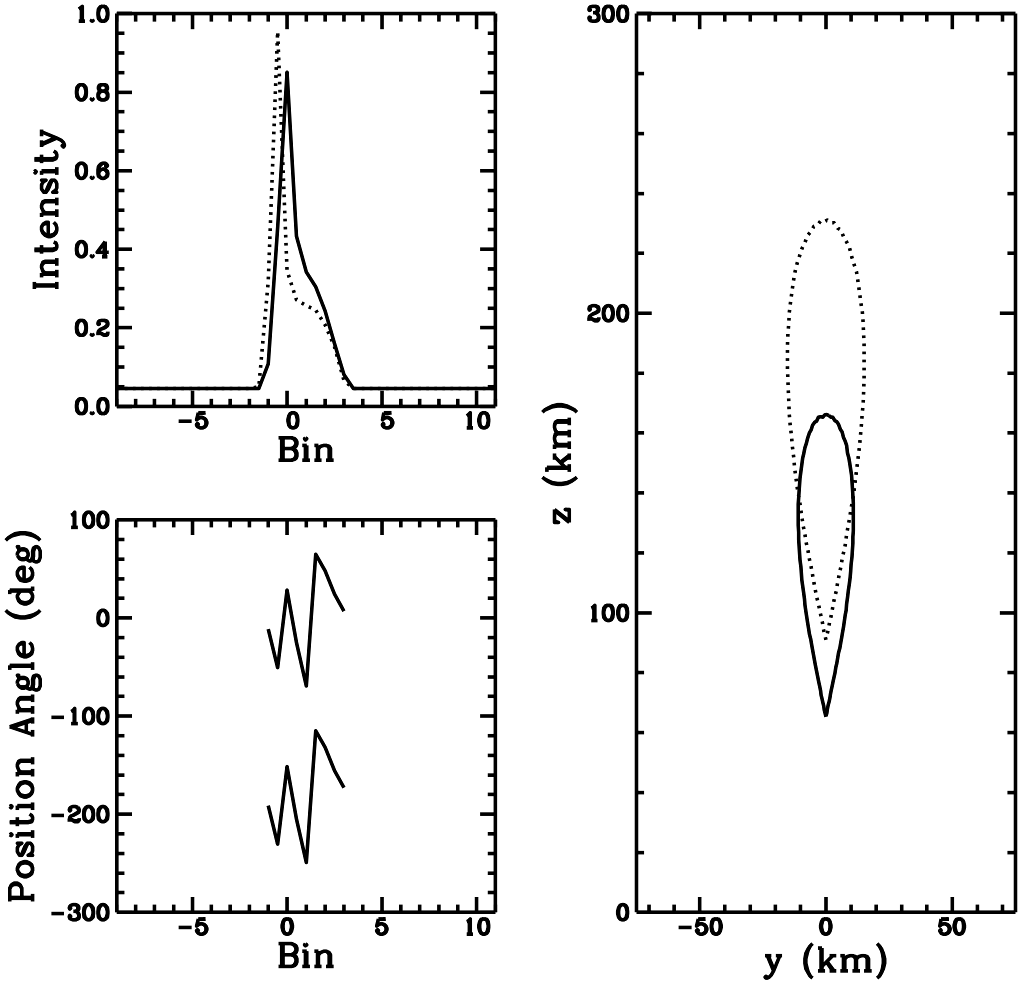

Figure 7.—This figure shows model-generated pulse profiles at 1.4 GHz (*dotted*) and 2.3 GHz (*solid*) and the corresponding transition surfaces. The pulse period consists of one hundred bins.

somewhat obscured by the break in the curve caused by the coarse graining of the bins. At the start of the pulse, the shape of the curve deviates from the S-shaped curve predicted by the simple rotating-vector model because rays from many longitudes contribute to the leading edge of the pulse.

Figure 8 shows the observed integrated pulse profile for the Vela pulsar at 1.4 GHz. The average position angle sweeps through roughly the same range for both profiles. More interesting, the predicted and observed profiles both appear to consist of the overlap of a strong subpulse followed by a weaker subpulse, although the model did not reproduce the relative strengths accurately. In our model, the presence of two subpulses arises from a combination of three effects.

Every ray reaching the observer emanates from a point on the stellar surface; therefore, we can map a pulse to a curve on the stellar surface. Moving along this curve corresponds to advancing in time on the profile. Typically, this path starts at some point $(\theta_0, \phi_0) = (\Theta_0, \Phi_0)$ and while ϕ_0 monotonically decreases, θ_0 first decreases, reaches a minimum, and then increases.

Because of the cylindrical symmetry around the magnetic pole, each circle of latitude on the stellar surface has an associated circle of transition points in the magnetosphere. The density of rays reaching the observer is higher when the line of sight grazes one of these circles than when it cuts across the circle at some angle. Hence, the density of rays reaches a peak when θ_0 hits its minimum and the path on the stellar surface is tangent to a circle of latitude.

Each ray represents an area element $d\Omega \approx \theta_0 d\theta_0 d\phi_0$, so its weight contains a factor of θ_0 as $d\theta_0$ and $d\phi_0$ are fixed in our model. The weight assigned to a ray also has the Gaussian factor mentioned earlier, representing the strength of the average beam. The beam is strongest at the magnetic pole and weakens away from the pole

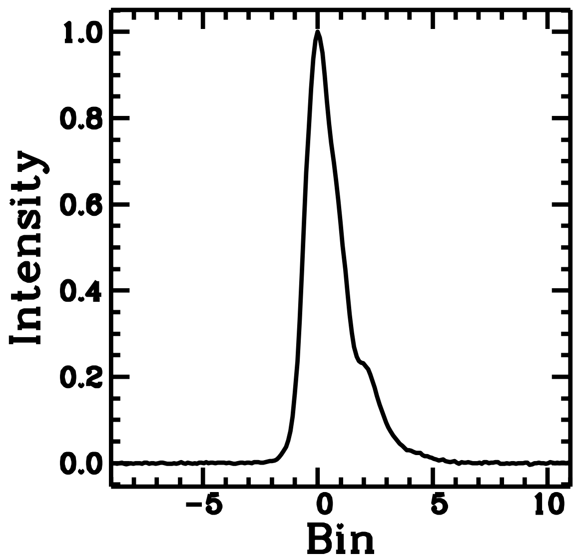

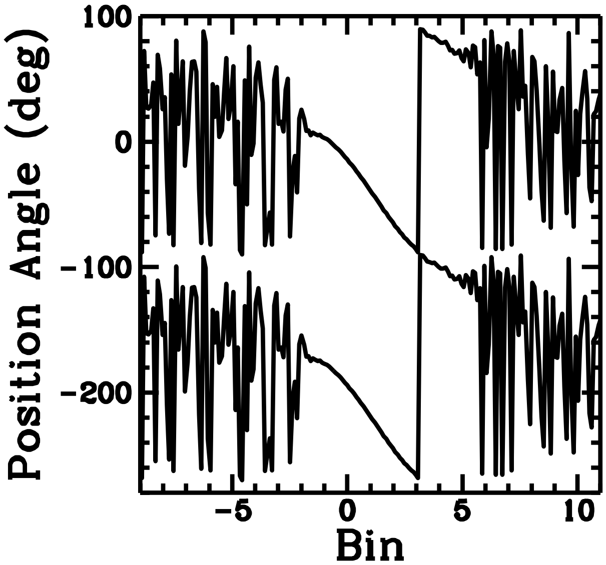

Figure 8.—The observed integrated pulse profile of the Vela pulsar at 1.4 GHz. We thank S. Sallmen and D. C. Backer for providing these data.

with a characteristic distance specified by σ_θ.

This combination of weighting factors can easily lead to the appearance of two subpulses. At first, when θ_0 is large, the Gaussian factor suppresses the weighting. As θ_0 decreases, the weighting at first steadily increases. At some point, the area factor θ_0 will begin to dominate, and the weight will decrease, resulting in the first subpulse. After θ_0 reaches its minimum, the reverse sequence occurs, generating the second subpulse.

Neither the higher density of rays at smaller values of θ_0 nor the weighting assigned to the rays can result in the observed pulse with its asymmetry between the two subpulses. Neither effect nor their combination breaks the cylindrical symmetry. If the density effect enhances one weighting maximum, it will enhance the other one equally. With only these two effects, the observer would always see a symmetrical pulse.

The final effect is the time-of-arrival effect, which does break the symmetry. In the corotating frame, the cylindrical symmetry about the magnetic pole results in a transition surface with a reflection symmetry through the *xz*-plane. The Lorentz boost to the observer's frame, however, breaks the symmetry by rotating all of the wave vectors in the direction of the boost and, because this rotation affects the time of arrival, skewing the pulse to the left in the profile. The other contribution to the time-of-arrival delay further skews the pulse to the left; rays from further out on the transition surface take less time to travel to the observer and arrive earlier in the pulse. Also because their transition points are moving faster, they undergo a larger boost, resulting in a larger rotation and causing them to arrive even earlier in the pulse.

Figure 9 illustrates how these effects combine to give the observed pulse. The top plot shows that rays starting near the magnetic pole arrive early in the pulse. The bottom plot shows the weighting with two maxima, but these small variations can not alone account for the large difference in strength between the two subpulses. The

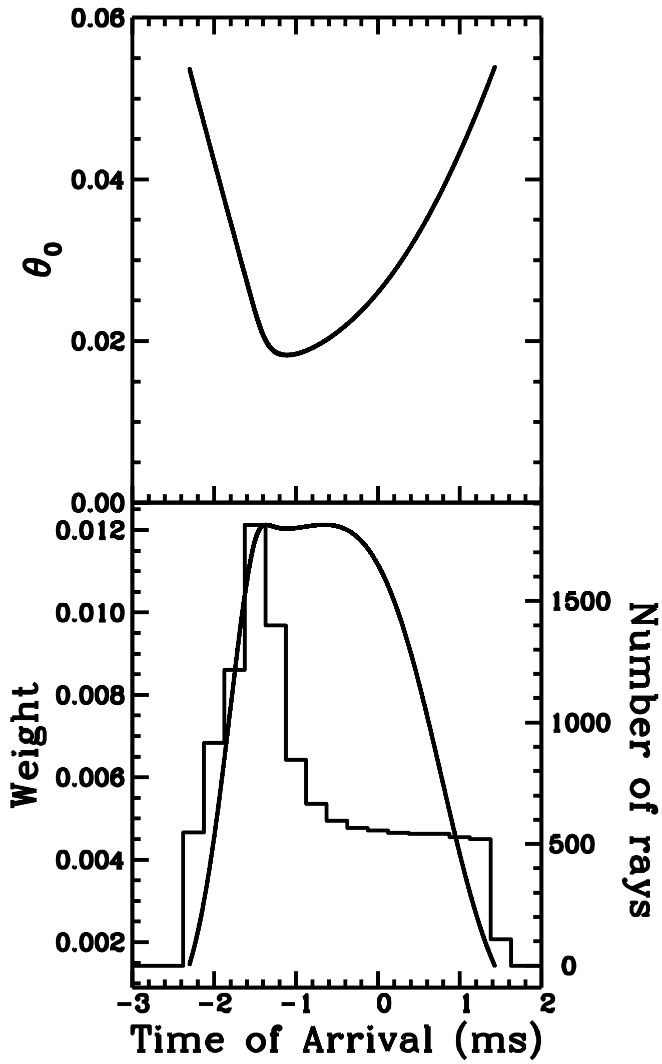

Figure 9.—Rays from near the magnetic pole arrive early in the pulse, enhancing the first subpulse.

superimposed histogram shows that many rays amass near the beginning of the profile. The first subpulse results then from a combination of the first maximum in the weighting and the large number of rays reaching the observer at the same time. The second subpulse arises as the rays arrive at a constant rate but with decreasing weights.

SUMMARY

A simple ray-tracing model that assumes a neutron star with a corotating dipolar magnetic field yields results which appear qualitatively consistent with observations. The resulting pulse profile exhibits the general characteristics of the observed profiles; the size of the emission region agrees with recent measurements; and the model naturally incorporates the rotating-vector model if one assumes the mode conversion process does not obliterate polarization information.

The basic nature of the model, moreover, leaves room for refinement. We have neglected the physics in the transition from the slow mode to the fast mode, and an improved model may involve a more realistic momentum distribution for the plasma. Finally, adjusting the weight assigned to each ray by incorporating a more detailed model of the radiation distribution at the surface may yield information about the shape of individual pulses and their variations.

APPENDIX

TRANSFORMATIONS FROM THE COROTATING FRAME TO THE OBSERVER'S FRAME

After solving equation (10) for r / r_0, we can find θ_f using equation (4). Due to the cylindrical symmetry of the dipole field, transitions occur for all values of ϕ. For a given value of ϕ, the transition occurs at the point

$$\mathbf{r} = r(\sin\theta_f \cos\phi, \sin\theta_f \sin\phi, \cos\theta_f), \tag{A1}$$

and the ray has a wave vector

$$\mathbf{k} = \omega(\sin\xi \cos\phi, \sin\xi \sin\phi, \cos\xi) \tag{A2}$$

where $\xi = (9/8)\theta_f$. The electric field $\mathbf{e}$ and magnetic field $\mathbf{b}$ are given by

$$\begin{aligned} \mathbf{e} &= (\cos\xi \cos\phi, \cos\xi \sin\phi, -\sin\xi) \\ \mathbf{b} &= (-\sin\phi, \cos\phi, 0) \end{aligned} \tag{A3}$$

We are working in units where $c = 1$. The vectors are normalized as we are not concerned with their magnitudes but only with their directions so that we can determine the polarization of the ray as seen by the observer.

The coordinates in the corotating frame and the observer's frame are related via two rotations so that

$$\begin{aligned} \mathbf{R} &= (X, Y, Z) = R_Z(\delta) R_Y(\iota)\mathbf{r} \\ \tilde{\mathbf{K}} &= (\tilde{K}_X, \tilde{K}_Y, \tilde{K}_Z) = R_Z(\delta) R_Y(\iota)\mathbf{k} \\ \tilde{\mathbf{E}} &= (\tilde{E}_X, \tilde{E}_Y, \tilde{E}_Z) = R_Z(\delta) R_Y(\iota)\mathbf{e} \\ \tilde{\mathbf{B}} &= (\tilde{B}_X, \tilde{B}_Y, \tilde{B}_Z) = R_Z(\delta) R_Y(\iota)\mathbf{b} \end{aligned} \tag{A4}$$

where R_Z and R_Y are the rotation matrices for rotations by the specified angles about the Z-axis and Y-axis respectively.

The vector $\tilde{\mathbf{K}}$ does not give the wave vector of the ray as seen by the observer; rather, it is the representation of the wave vector as measured in the corotating frame expressed in the coordinates of the observer's frame. To find the wave vector as seen by the observer, we must apply a Lorentz transformation because the transition point moves with a velocity $\beta = (\Omega\hat{\mathbf{Z}}) \times \mathbf{R} / c$.

The components of $\tilde{\mathbf{K}}$ parallel and perpendicular to β are given by

$$\begin{aligned} \tilde{\mathbf{K}}_{\parallel} &= (\tilde{\mathbf{K}} \cdot \hat{\beta})\hat{\beta} \\ \tilde{\mathbf{K}}_{\perp} &= \tilde{\mathbf{K}} - \tilde{\mathbf{K}}_{\parallel} \end{aligned} \tag{A5}$$

where $\hat{\beta}$ denotes the unit vector in the direction of β. According to the observer, the ray has a wave vector $\mathbf{K} = \mathbf{K}_{\perp} + \mathbf{K}_{\parallel}$ where

$$\begin{aligned} \mathbf{K}_{\parallel} &= \gamma(\tilde{K}_{\parallel} + \beta\omega)\hat{\beta} \\ \mathbf{K}_{\perp} &= \tilde{\mathbf{K}}_{\perp} \end{aligned} \tag{A6}$$

and $\gamma = 1 / \sqrt{1 - \beta^2}$ is the usual relativistic factor.

We must likewise transform the electric and magnetic fields. The electric and magnetic fields that the observer will see are given by

$$\begin{aligned} \mathbf{E} &= \gamma(\tilde{\mathbf{E}} - \beta \times \tilde{\mathbf{B}}) - \frac{\gamma^2}{\gamma + 1}(\beta \cdot \tilde{\mathbf{E}})\beta \\ \mathbf{B} &= \gamma(\tilde{\mathbf{B}} + \beta \times \tilde{\mathbf{E}}) - \frac{\gamma^2}{\gamma + 1}(\beta \cdot \tilde{\mathbf{B}})\beta \end{aligned} \tag{A7}$$

The position angle ψ is then given by

$$\psi = \tan^{-1}\left(\frac{E_y}{\sqrt{E^2 - E_Y^2}}\right) \tag{A8}$$

REFERENCES

Arons, J., & Barnard, J. J. 1986, *ApJ*, 302, 120

Backer, D. C., Rankin, J. M., & Campbell, D. B. 1976, *Nature*, 263, 202

Barnard, J. J., & Arons, J. 1986, *ApJ*, 302, 138

Beskin, V. S., Gurevich, A. V., & Istomin, I. N. 1988, *Ap&SS*, 146, 205

Cheng, A. F., & Ruderman, M. A. 1979, *ApJ*, 229, 348

Cordes, J. M. 1978, *ApJ*, 222, 1006

Goldreich, P. & Julian, W. H. 1969, *ApJ*, 157, 869

Gallant, Y. A. 1996, in IAU Colloq. 160, *Pulsars: Problems and Progress*, ed. S. Johnston, M. A. Walker, & M. Bailes (San Francisco: Astronomical Society of the Pacific), 431

Gwinn, C. R., Britton, M. C., Reynolds, J. E. J., Jauncey, D. L., King, E. A., McCulloch, P. M., Lovell, J. E., Flanagan, C. S., & Preston, R. A. 2000, *ApJ*, 531, 902

Krishnamohan, S., & Downs, G. S. 1983, *ApJ*, 265, 372

Lerche, I. 1970, *ApJ*, 162, 153

Lyne, A. G., & Graham-Smith, F. 1998, *Pulsar Astronomy*, (2nd ed.; Cambridge: Cambridge University Press)

Lyutikov, M. 1998, Ph.D. Dissertation, California Institute of Technology

Macquart, J. P., Johnston, S., Walker, M., & Stinebring, D. 1999, in IAU Colloq. 177, *Pulsar Astronomy---2000 and Beyond*, ed. M. Kramer, N. Wex, & R. Wielebinski (San Francisco: Astronomical Society of the Pacific), 215

Manchester, R. N. 1975, *Proceedings of the Astronomical Society of Australia*, 2, 334

McKinnon, M. M., & Stinebring, D. R. 1998, *ApJ*, 502, 883

Melrose, D. B. 1996, in IAU Colloq. 160, *Pulsars: Problems and Progress*, ed. S. Johnston, M. A. Walker, & M. Bailes (San Francisco: Astronomical Society of the Pacific), 139

Radhakrishnan, V., & Cooke, D. J. 1969, *Astrophys. Lett.*, 3, 225

Rankin, J. M. 1983, *ApJ*, 274, 333

Scintillation Parameters for PSR J0437-4715

C. Hirano and C. R. Gwinn
Department of Physics, University of California, Santa Barbara, CA 93106

Submitted to *The Astrophysical Journal*.

ABSTRACT

We present revised estimates of the decorrelation bandwidth and scintillation time scale for PSR J0437-4715 and find that the scattering occurs at the surface of the Local Bubble. Our results, derived from interferometric observations of PSR J0437-4715 at two epochs, do not scale with observing frequency as expected for interstellar scattering in comparison with results reported by other groups observing at different frequencies and times. This disagreement may suggest that a different scaling law applies or that the parameters vary with time; however, we also detect evidence of fine structure on a scale which appears to agree roughly with the earlier measurements. We propose that misidentification of such fine structure as the fundamental scintillation pattern may be common among nearby pulsars, and that this could provide at least a partial explanation for the discontinuity in the scaling of temporal broadening with dispersion measure for pulsars with measured scattering properties.

INTRODUCTION

Fluctuations in the electron density in the interstellar medium (ISM) scatter electromagnetic radiation from a source such as a pulsar, giving rise to the phenomenon of interstellar scintillation (ISS). While some models explore scattering in an extended medium, simplified models typically assume that radiation from the source scatters off a thin screen located between the source and observer. Rays may reach an observer via multiple paths, and the resulting interference creates a diffraction pattern in the observing plane.

Scintillation causes the intensity of the source to vary with time and frequency. The time variations arise from motions of the source and screen relative to the observer which cause the scintillation pattern to move relative to the observer with scintillation velocity V_{ISS}. In the frequency domain, scintillation maxima have finite widths as the conditions which result in constructive interference at one frequency result in destructive interference at a sufficiently different frequency. The two observables, the scintillation time scale t_{ISS} and decorrelation bandwidth $\Delta\nu_{ISS}$, characterize the size of the maxima in, respectively, the time and frequency domains.

Models of the ISM predict how these two observables scale with observing frequency ν, and for interstellar scattering, we expect $\Delta\nu_{ISS} \propto \nu^{4.4 \text{ to } 4}$ and $t_{ISS} \propto \nu^{1.2 \text{ to } 1}$. In the widely accepted Kolmogorov model, the power spectrum of the electron density fluctuations is given by

$$P(\mathbf{q}) = C_n^2 |\mathbf{q}|^{-11/3} \qquad \frac{2\pi}{l_o} \leq |\mathbf{q}| \leq \frac{2\pi}{l_i} \tag{1}$$

which holds between an inner length scale l_i and outer length scale l_o. C_n denotes the level of density fluctuations, and $\mathbf{q}$, the wave vector. With this model, we expect that $\Delta\nu_{ISS} \propto \nu^{4.4}$ and $t_{ISS} \propto \nu^{1.2}$.

From these observables, one can infer the scintillation velocity V_{ISS} via the relation (Gupta et al. 1994)

$$V_{ISS} = A_V \frac{\sqrt{\Delta\nu_{\mathrm{MHz}} D_{\mathrm{kpc}} x}}{\nu_{\mathrm{GHz}} t_{ISS}} \ \mathrm{km\ s^{-1}} \tag{2}$$

Here $\Delta\nu_{\mathrm{MHz}}$ is the decorrelation bandwidth in megahertz; D_{kpc} is the distance to the pulsar in kiloparsecs; t_{ISS} is the scintillation time scale in seconds; and ν_{GHz} is the observing frequency in gigahertz. Traditionally, the parameter $x = d_s / (D - d_s)$, where D is the observer-to-pulsar distance and d_s is the observer-to-screen distance, is taken to be unity; in other words, the scattering screen is assumed to be halfway between the observer and the pulsar. The numerical factor A_V is a model-dependent constant. Lyne & Smith (1982) used a value of 2×10^4 while Cordes (1986) and Harrison & Lyne(1993) used a value of 1.27×10^4. Gupta et al. subsequently derived a new estimate for A_V of 3.85×10^4, which is the value we adopt in our analysis.

From the scintillation velocity V_{ISS}, one can infer the velocity of the pulsar using a lever-arm argument. Studies by Lyne & Smith, Cordes, and Gupta et al. compared velocities derived from scintillation methods with those measured using other methods and found the two sets of results were correlated. Scintillation methods, however, systematically underestimated the proper motion of pulsars (Harrison & Lyne). Gupta (1995) reexamined the correlation using the revised value of A_V and taking into account revisions to the pulsar distance scale (Taylor & Cordes 1993) and found that the systematic bias disappeared and that the two sets of results agreed quite well statistically.

One may infer the broadening time τ_s from the decorrelation bandwidth $\Delta\nu_{ISS}$ via the uncertainty relation

$$\Delta\nu_{\mathrm{ISS}}\tau_s = \frac{C_1}{2\pi} \tag{3}$$

where the constant C_1 depends on the scattering model and on the particular definitions of $\Delta\nu_{ISS}$ and τ_s. For their pulsar catalog, Taylor, Manchester, & Lyne (1993) used a value of $C_1 = 1.53$. Lambert & Rickett (1999) subsequently argued that for a thin-screen geometry this value of C_1 results in overestimates of the broadening time by a factor of 2.34. We therefore use $C_1 = 0.654$ in our analysis.

Simple scattering models suggest that temporal broadening should depend approximately quadratically on dispersion measure *DM*; observation, however, shows that for large dispersion measures, $\tau_s \propto DM^{4.4}$, as shown in Figure 1 (Lyne & Graham-Smith 1998). The cutoff between the two regimes appears to occur around $DM \approx 30\ \mathrm{cm}^{-3}$ pc.

With its low dispersion measure of $DM = 2.6484\ \mathrm{cm}^{-3}$ pc, PSR J0437-4715 lies at left end of Figure 1, providing us with one compelling reason to observe this particular pulsar as we were interested in seeing if the pulsar followed the trend of other low-*DM* pulsars. PSR J0437-4715 also has a well-defined bow shock (Fruchter 1998), and its strength and proximity, at a distance of 180 pc (Sandhu et al. 1997), make it a good candidate to probe the local ISM. The bow shock and the surface of the Local Bubble are two regions which could conceivably dominate the scattering behavior of the pulsar (Britton 1996).

OBSERVATIONS AND ANALYSIS

DATA COLLECTION AND CALIBRATION

We observed PSR J0437-4715 at two epochs using the Very Long Baseline Array (VLBA) operated by the National Radio Astronomy Observatory (NRAO). On 5 November 1996, we observed the pulsar over four 33-minute scans, using 25-meter telescopes at Fort Davis, Mauna Kea, Pie Town, and St. Croix, with a 32-MHz bandwidth centered at 332 MHz, and with a 250-kHz spectral resolution. Between the scans, we observed extragalactic sources for calibration purposes. On 8 April 1999, we observed the target for two 44-minute scans and one 33-minute scan, using the

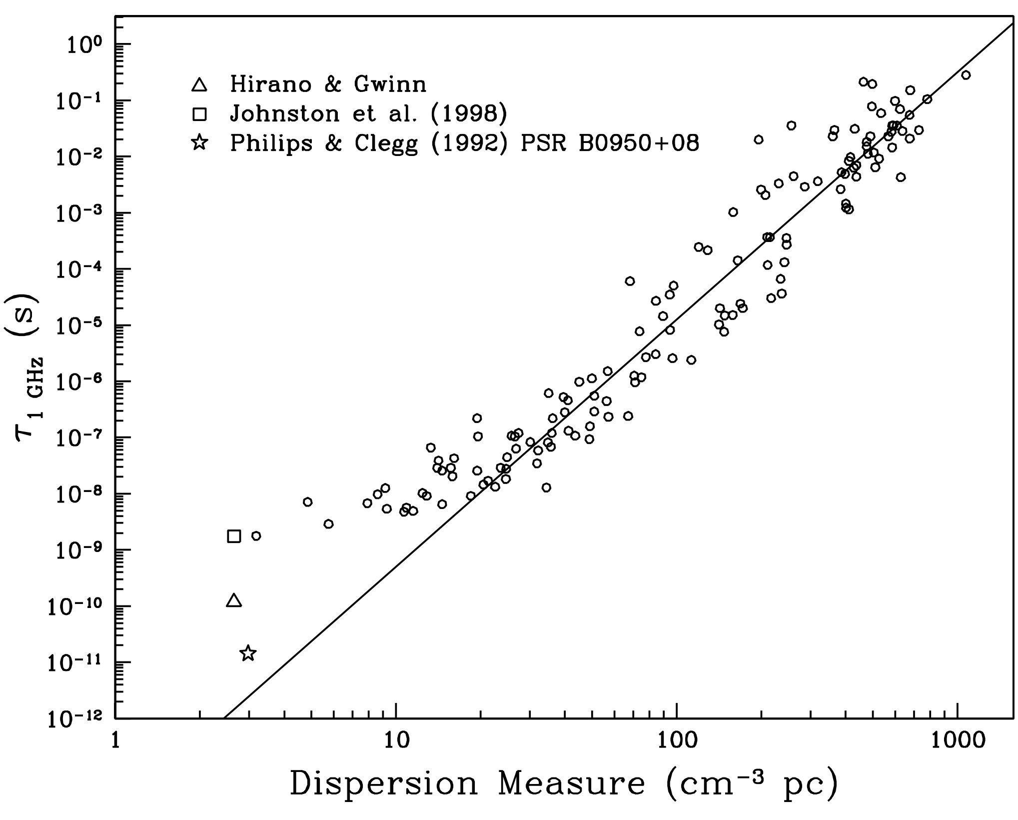

Figure 1.—The relationship between temporal broadening and dispersion measure. Except as noted, the data were taken from Taylor et al.

telescopes at Fort Davis, Kitt Peak, Los Alamos, Mauna Kea, Owens Valley, Pie Town, and St. Croix, with a bandwidth of 32 MHz centered at 328 MHz, and with a spectral resolution of 125 kHz. To increase the signal-to-noise ratio, the data for this observation were correlated using a gate which covered 12% of the pulse period and which isolated the central peak of the pulse profile. Scans of a calibrator source preceded and succeeded the observations of the pulsar. For both observations, we aggregated the 32-MHz bandwidth using four 8-MHz intermediate-frequency (IF) bands.

We performed half of the calibration using NRAO's Astronomical Image Processing System (AIPS). The data from both observations were marred by radio-frequency interference (RFI). The second observation in particular suffered badly from RFI, forcing us to eliminate the Kitt Peak and Owens Valley antennas from the outset. The interference also tainted some of the measurements of the system temperature. The system temperature should not change abruptly, so if an isolated reading clearly departed from an otherwise smooth trend, we merely removed that value. In two IFs, however, rampant corruption due to RFI obliterated evidence of a smooth evolution in system temperature. For these two IFs, we copied the system temperatures from an adjacent IF, as system temperatures should not vary wildly from IF to IF.

We examined the remaining visibilities and flagged channels and time ranges to eliminate data corrupted by very strong, narrow-band signals typical of man-made sources. We applied the usual corrections for the effects of antenna parallactic angles, digital sampler bias, system temperature, and gain calibration. We then performed a manual phase calibration by running a fringe fit on a thirty-second interval of calibrator data to determine the electronic delay differences between IFs, and we removed the resulting phase differences from the pulsar and calibrator data. The final procedure done using AIPS was a fringe fit on each source to remove phase slopes due to the residual fringe rate and delay.

To perform a bandpass calibration, we averaged, for each baseline, the complex visibilities from a ten-minute interval of calibrator data. Deviations from a flat amplitude and phase spectrum reflected the non-ideal frequency response of the baseband converters. The gain of the filters drops off at the ends of each IF, significantly reducing the signal-to-noise ratio in the first and last channel of each IF; consequently, we omitted these channels in our subsequent analysis. We then smoothed the data using boxcar averaging with a one-minute window to further increase the signal-to-noise ratio.

At our observing frequency, propagation through the ionosphere significantly affects the visibility phases (Thompson, Moran, & Swenson 1986). The fringe fit to remove the residual fringe rate eliminated the linear dependence of phase on time, but significant higher-order terms remained. Data from both observations exhibited broadband variations in phase of order half a radian over a time scale of about fifteen minutes, as would be expected for weak scattering in the ionosphere. We approximated and removed these variations using an eighth-order polynomial fit to amplitude-weighted phase averages calculated for each time point.

The ionosphere also induced phase curvature in frequency. The fringe fit removes the first-order dependence of phase on frequency, and usually, the bandwidth is small enough compared to the observing frequency that the second-order term is not important. However, in our case, the bandwidth was approximately 10% of the observing frequency, and the resulting 1% correction could be of order a radian for typical values of total electron content for the ionosphere. We fit the amplitude-weighted phase averages calculated for each channel to a quadratic polynomial and used this polynomial to calculate the appropriate phase to subtract from the visibilities in each channel.

To verify that our calibration procedure did not introduce any unintended biases, we calculated two-dimensional autocorrelation functions (ACF) for each data set using the visibilities from a calibrator source. As expected, we obtained results flat in both time and frequency lags, except for a spike at small time and frequency lags due to the effects of noise.

DATA ANALYSIS

Initially, we had hoped to measure the angular broadening of the pulsar by measuring the phase variations of the diffraction pattern; however, several complications derailed our efforts. Most significant, the decorrelation bandwidth was much larger than expected. As the phase variations of the diffraction pattern have this characteristic bandwidth (Desai et al. 1992), they could not be distinguished from ionospheric phase, phase slope, and curvature. Furthermore, we did not obtain fringes on the longest baseline where we expect phase variations of the diffraction pattern to be largest.

The remaining baselines were of comparable lengths, so we chose to focus on the Fort Davis-Pie Town baseline. Figure 2 shows plots of the visibility amplitudes for the pulsar on this baseline for both epochs. The white vertical lines correspond to the channels omitted at the ends of each IF, and the white horizontal lines correspond to breaks in the scan or to time ranges flagged because of RFI. At both epochs, we detected scintillation maxima that typically persist for ten to twenty minutes and that

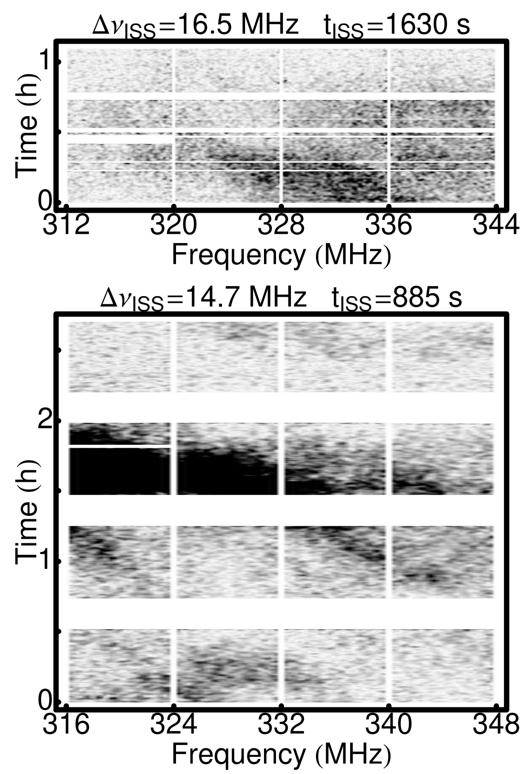

Figure 2.—These plots show the visibility amplitude as a function of frequency and time for observations of PSR J0437-4715 on the Fort Davis-Pie Town baseline on 5 November 1996 (bottom) and 8 April 1999 (top).

span several IFs, suggesting a characteristic width in frequency on the order of ten megahertz.

Gwinn et al. (1998) showed that for a Gaussian spectrum of density fluctuations, the ACF for zero time lag on a baseline **b** has the form

$$\langle C^*(\nu, t) C(\nu + \Delta\nu, t) \rangle \propto \overline{V}(\mathbf{b})^2 + \frac{1}{1 + (\Delta\nu / \Delta\nu_{\mathrm{ISS}})^2} \qquad (4)$$

where $\overline{V}(\mathbf{b}) = \exp[-(k\theta b)^2 / 2]$ is the average normalized visibility. Here k is the wave number; b is the baseline length; and θ is the angular size of the scattering disk, which is of order milliarcseconds. The length scale $1 / k\theta$ is of order 10^4 km and is larger than the diameter of the Earth; in particular, it is much greater than 565 km, the length of the Fort Davis-Pie Town baseline. Hence, $k\theta b \ll 1$ and

$$\langle C^*(\nu, t) C(\nu + \Delta\nu, t) \rangle = 1 + \frac{1}{1 + (\Delta\nu / \Delta\nu_{\mathrm{ISS}})^2} \qquad (5)$$

The small deviations from this form for a Kolmogorov or other plausible non-Gaussian spectrum would not affect our fitted results.

To determine the decorrelation bandwidth, we calculated the two-dimensional ACFs for the Fort Davis-Pie Town baseline. Figure 3 shows the amplitude of one such ACF, with the noise spike removed. The contours divide the range of the function into ten equally sized intervals. We fit the time-lag axis of the two ACFs to the form given in equation (5). To each point used in the fit, we assigned a weight equal to the square root of the number of pairs used to calculate that point. The fits

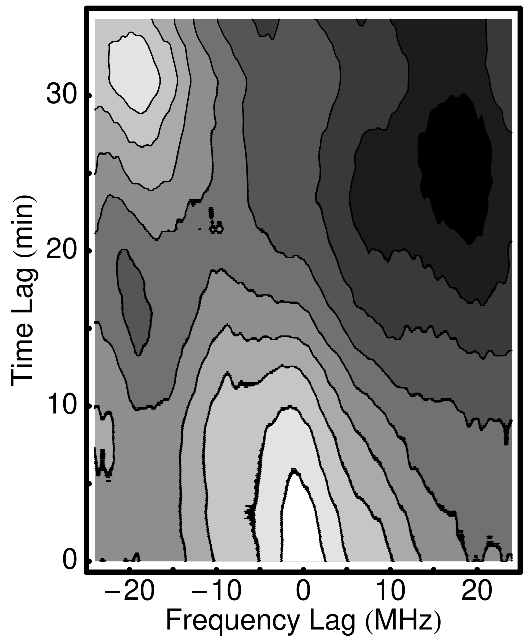

Figure 3.—A contour plot of the two-dimensional ACF amplitude obtained for the Fort Davis-Pie Town baseline.

yielded a decorrelation bandwidth of 14.7 ± 0.5 MHz for the first epoch and 16.5 ± 0.5 MHz for the second. The uncertainties represent the 95%-confidence level of the fits.

Neither epoch individually provided a correlation function with a form particularly close to that given in equation (5); however, the composite ACF obtained by suitably combining the two individual functions did. To combine the two functions, we first halved the spectral resolution of the second-epoch function by averaging two adjacent bins, weighted according to the number of contributing pairs, into one bin, and then we averaged the two ACFs together bin by bin, again assigning weights proportional to the number of pairs contributing to a bin. The resulting

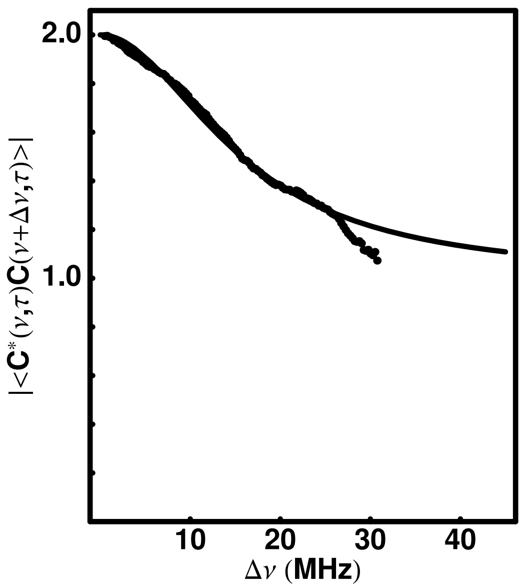

Figure 4.—The composite ACF obtained by suitably combining the ACFs from the two observations. The best-fitting Lorentzian has a characteristic width of 15.7 ± 0.2 MHz.

function, shown in Figure 4, matched the theoretical prediction well. The solid line shows the best-fit results, from which we obtained a decorrelation bandwidth of 15.7 ± 0.2 MHz. Again, the uncertainty represents a 95%-confidence level.

To estimate the scintillation time scale, we fit the correlation function along the time-lag axis to a Gaussian plus an offset. The parameters of the fit were the offset and the amplitude and width of the Gaussian. The scintillation time scale is traditionally defined to be the time at which the Gaussian component of the correlation function declines to 1 / *e* of its maximum value. The fits yielded estimates of 885 ± 9 s for the first epoch, 1630 ± 80 s for the second, and 1020 ± 70 s for the composite ACF.

DISCUSSION

SCINTILLATION BANDWIDTH

COMPARISON WITH PREVIOUS RESULTS

Figure 5 shows measurements of the decorrelation bandwidth $\Delta\nu_{ISS}$ and scintillation time scale t_{ISS} for observations of PSR J0437-4715, rescaled to an observing frequency of 330 MHz. The horizontal lines indicate the equivalent observing bandwidth for each measurement. Our estimates of $\Delta\nu_{ISS}$ agree with a

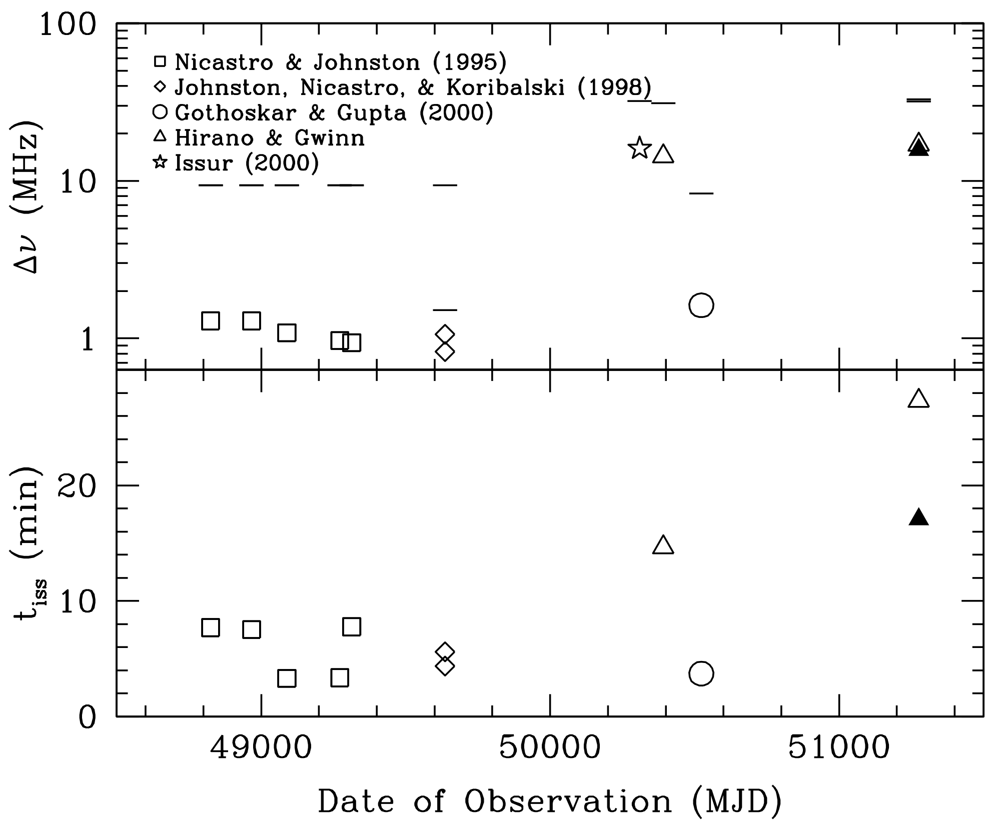

Figure 5.—Measurements of the decorrelation bandwidth and scintillation time scale plotted against observing date. The horizontal lines indicate the effective bandwidth used for each measurement. The solid triangles show our estimates of $\Delta\nu_{ISS}$ and t_{ISS} derived from the composite ACF.

decorrelation bandwidth of 0.5 $\pm$ 0.1 MHz at 150 MHz obtained by Issur (2000), but they clearly do not agree with the results reported by Nicastro & Johnston (1995), Johnston, Nicastro, & Koribalski (1998), and Gothoskar & Gupta (2000). Our estimates of the scintillation time scale are also inconsistent with earlier measurements.

One possible explanation for the discrepancy is that the nature of the scattering changes significantly with time. Bhat (1999) observed that scintillation parameters often vary with time. Pulsars generally move with high speeds and therefore the line of sight to a pulsar may pass through regions of widely varying electron density on relatively short time scales. Rays from distant pulsars must still travel through many density fluctuations; consequently, any effect due to the pulsar's motion will tend to average out. However, the proximity of nearby pulsars like PSR J0437-4715 reduces the number of independent regions so that one might expect to see the scintillation parameters change significantly with time.

Gothoskar & Gupta found a decorrelation bandwidth of 1.56 MHz at an observing frequency of 327 MHz, consistent with the earlier results, from data taken 130 days after our first observation. Such a significant change over this time period would suggest that the scattering occurs in a small region close to the pulsar. On the other hand, Nicastro & Johnston observed PSR J0437-4715 at 436 MHz at five epochs over a 488-day period and did not see a dramatic shift in the decorrelation bandwidth.

Another possibility is that we are measuring different parameters than those in the earlier observations. The effective bandwidth of earlier observations corresponds to the width of one of our IFs, and as seen in Figure 5, our points lie outside this bandwidth because, as seen in Figure 2, a scintillation maximum typically spans several IFs. If the decorrelation bandwidth scales as expected with observing frequency, the earlier experiments may have detected evidence of structure within an intensity maximum that covered the entire observing bandwidth.

VLBI observations have an advantage over single-dish observations in these cases. In VLBI, because the receiver noise of the antennas are independent of each other, the average visibility will vanish when the signal vanishes; hence, we can easily tell whether or not the scintillation intensity goes to zero even when the intensity maximum encompasses nearly the entire bandwidth. In single-dish experiments, the receiver noise must be manually separated from the signal, allowing for the possibility that part of the signal is misidentified as noise.

FINE-SCALE STRUCTURE WITHIN SCINTILLATION MAXIMA

Figure 6 shows an expanded view of a scintillation maximum. We found that the amplitude varies within the maximum with a modulation index of approximately 0.2. The variations appear to occur with a characteristic bandwidth of order 1 MHz and on a time scale of a few minutes. Interestingly, these figures would agree with the estimates of the scintillation bandwidth and time scale from the earlier observations.

The small characteristic bandwidth seems to conflict with the small modulation index. A small bandwidth suggests strong scattering while the small

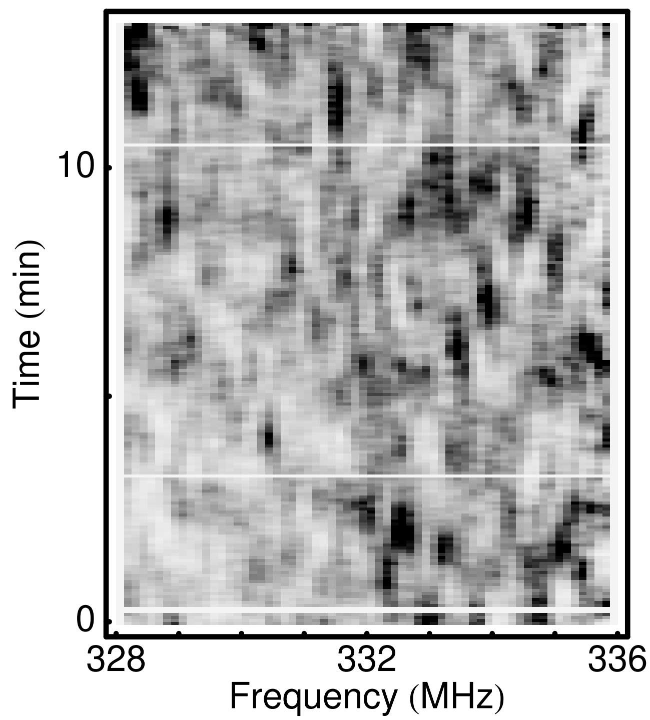

Figure 6.—Variations in the visibility amplitude within a scintillation maximum appear to occur over a frequency scale on the order of 1 MHz.

modulation index suggests weak scattering. We surmise that the fine structure arises due to a multiple-imaging phenomenon. Cordes & Wolszczan (1986) and recently Stinebring et al. (2001), for example, have shown that multiple imaging of pulsars account for secondary features, such as multiple drift slopes, in pulsar dynamic spectra. We discuss in a separate paper more fully how the variations we detected may arise.

TEMPORAL BROADENING OF NEARBY PULSARS

Our estimate of the decorrelation bandwidth corresponds to a broadening time of $\tau_s = 5.0\times10^{-11}$ s at 1 GHz. (Because τ_s is less than the wave period at 1 GHz, τ_s should be viewed simply as a parameter and not the actual pulse broadening observable at that frequency.) As seen in Figure 1, our relatively large result for the decorrelation bandwidth and consequently small estimate of the broadening time moves PSR J0437-4715, despite its small dispersion measure, significantly toward the trend followed by pulsars with large dispersion measures; the previous estimates, in contrast, suggest that the pulsar behaves like a typical low-*DM* pulsar. PSR B0950+08, which has a dispersion measure of 2.9702 cm^{-3} pc, also follows the trend of pulsars with large dispersion measures, based on measurements by Phillips & Clegg (1992). Observing at 47 MHz and 51 MHz, they also found a decorrelation bandwidth much larger than expected and attributed underestimates of the decorrelation bandwidth at higher frequencies to insufficient observing bandwidth at those frequencies.

We suggest that other pulsars, particularly those with low DM, may have temporal broadening significantly smaller than represented in the literature and in Figure 1. This may remove the change in power-law index visible as a change in slope on the log-log scale of Figure 1. For both PSR B0950+08 and PSR J0437-4715, observations at lower frequencies and wider bandwidth resulted in sharp upward revisions of the decorrelation bandwidth, leading to sharp downward revisions of the inferred temporal broadening τ_s. For PSR B0950+08, earlier observations had reported intensity variations with frequency and time that varied greatly between observing epochs and often did not resemble that expected from scintillation

(Armstrong & Rickett 1981, Roberts & Ables 1982, Cordes et al. 1985, Smirnova & Shabanova 1992). Phillips & Clegg, with observations at 50 MHz, showed that these variations were much narrower in bandwidth and shorter in time scale than the actual scintillations. Similarly for PSR J0437-4715, we describe above how observations at higher frequencies and narrower bandwidth may have misinterpreted fine structure within the diffraction pattern as scintillations. Stinebring et al. find that fine structure in the scintillation pattern occurs commonly among nearby pulsars. For such pulsars, temporal broadening is inferred from measurements of decorrelation bandwidth $\Delta\nu_{ISS}$. Therefore, we suggest that misidentification of fine structure as the fundamental scintillation pattern could be common among such pulsars and could move at least some of the pulsars at *DM* of 30 cm^{-3} pc or less in Figure 1 to lower τ_s. We propose that this might provide an instrumental explanation for the “kink" in that figure, rather than the more traditional explanation in terms of multiple phases of scattering material (Sutton 1971).

MEASURE OF TURBULENCE IN THE LOCAL ISM

Based on work by Cordes et al., Phillips & Clegg estimated the parameter C_n^2 in equation (1) using the relation

$$C_n^2 \ = \ 2{\times}10^{-6} \nu_{\mathrm{MHz}}^{11/3} D_{\mathrm{pc}}^{-11/6} \Delta\nu_{\mathrm{kHz}}^{-5/6} \ \mathrm{m}^{-20/3} \tag{6}$$

where ν_{MHz} is the observing frequency in megahertz, D_{pc} is the pulsar distance in parsecs, and $\Delta\nu_{\mathrm{kHz}}$ is the decorrelation bandwidth in kilohertz. For PSR B0950+08, they found values of $\log C_n^2$ ranging from -4.4 to -4.7 and noted that these values were significantly smaller than estimates obtained for other nearby pulsars, where the least scattered pulsars had values of $\log C_n^2$ close to -3.5.

For PSR J0437-4715, we find $\log C_n^2 = -4.1$, a value which is higher than what Phillips & Clegg found but lower than those for the other nearby pulsars. Because our observing bandwidth is only twice the decorrelation bandwidth, we may be underestimating the true decorrelation bandwidth; a larger decorrelation bandwidth would further lower our estimate of C_n^2, bringing it closer to the values found for PSR B0950+08.

SCINTILLATION VELOCITY

The scintillation velocity should equal the proper motion velocity if the scattering screen is located midway between the observer and source. Using equation (2) with $x = 1$ and $D = 0.180$ kpc, we calculated a scintillation velocity of $V_{ISS} = 192$ km s^{-1}, which agrees with previous measurements of the scintillation velocity. Johnston et al. obtained a value of 170 km s^{-1} from observations at 436 MHz, and Gothoskar & Gupta measured a mean scintillation velocity of 231 km s^{-1} from observations at 327 MHz. Proper motion measurements, however, have yielded significantly lower results. Bell et al. (1995) found a velocity of 91 ± 3 km s^{-1}, and Toscano et al. (1999), using arrival-time methods, recently obtained a velocity measurement of 120.5 ± 0.2 km s^{-1}. This disparity suggests that the assumption that $x = 1$ is not valid for PSR J0437-4715.

With the accuracy of scintillation methods established from measurements on other pulsars, we used this disparity to infer the distance to the scattering screen. The proper motion velocity of the pulsar V_{pm}, the scintillation velocity V_{ISS}, and the relative location of the scattering screen are related by

$$\left(\frac{V_{ISS}}{V_{pm}}\right)^2 \approx x = \frac{d_s}{D - d_s} \quad (7)$$

under the assumption that the velocity of the scattering material is negligible. Setting $V_{pm} = 120.5 \text{ km s}^{-1}$, we find that the scattering material is located at a distance $d_s = 129$ pc.

Gothoskar & Gupta likewise noted that the fact that the scintillation velocity for PSR J0437-4715 significantly exceeds the proper motion of the pulsar indicates that the scattering occurs relatively close to the pulsar. Their analysis suggests that the scattering primarily occurs on the shell of the Local Bubble, which, they estimate, lies at a distance of approximately 120 pc along this line of sight. Our estimate of the distance to the scattering screen agrees well with their hypothesis.

SUMMARY

From interferometric observations of PSR J0437-4715, we estimate the scintillation time scale to be $t_{ISS} = 1020$ s, the decorrelation bandwidth to be $\Delta\nu_{ISS} = 15.7$ MHz at 330 MHz, and the pulse broadening time to be $\tau_s = 5.0\times10^{-11}$ s at 1 GHz. These results disagree with previously reported values. We offer a possible explanation for this discrepancy: the earlier observations, because of limited bandwidth, detected evidence of structure within scintillation maxima. And, in fact, our data appear to exhibit such modulation on frequency and time scales consistent with the previously reported values of the scintillation bandwidth and time scale. We propound that, because of limited observing bandwidth, scintillation measurements at higher frequencies may systematically underestimate the true value of the decorrelation bandwidth of nearby pulsars, leading to the change in power-law index apparent in Figure 1.

From our parameters, we find that the diffraction pattern moves with speed $V_{ISS} = 192$ km s^{-1}, which agrees with previous estimates of the scintillation velocity but which significantly exceeds measurements of the pulsar's proper motion. We infer from this disparity that the scattering screen lies at a distance of 129 pc from the Earth and identify the screen with the surface of the Local Bubble.

ACKNOWLEDGMENTS

We thank A. Deshpande and N. Issur for helpful communications of their observations of PSR J0437-4715, and the National Science Foundation for financial support.

REFERENCES

Armstrong, J. W., & Rickett, B. J. 1981, *MNRAS*, 194, 623

Bell, J. F., Bailes, M., Manchester, R. N., Weisberg, J. M., & Lyne, A. G. 1995, *ApJ*, 440, L81

Bhat, N. D. R., Rao, A. P., & Gupta, Y. 1999, *ApJS*, 121, 483

Britton, M. C. 1996, Ph.D. Dissertation, University of California, Santa Barbara

Cordes, J. M., Weisberg, J. M., & Boriakoff, V. 1985, *ApJ*, 288, 221

Cordes, J. M. 1986, *ApJ*, 311, 183

Cordes, J. M., & Wolszczan, A. 1986, *ApJ*, 307, L27

Desai, K. M., Gwinn, C. R., Reynolds, J. R., King, E. A., Jauncey, D., Flanagan, C., Nicolson, G., Preston, R. A., & Jones, D. L. 1992, *ApJ*, 393, L75

Fruchter, A. S. 1998, http://icarus.stsci.edu/~fruchter/nebula/nebula.html

Gothoskar, P., & Gupta, Y. 2000, *ApJ*, 531, 345

Gupta, Y., Rickett, B. J., & Lyne, A. G. 1994, *MNRAS*, 269, 1035

Gupta, Y. 1995, *ApJ*, 451, 717

Gwinn, C. R., Britton, M. C., Reynolds, J. E. J., Jauncey, D. L., King, E. A., McCulloch, P. M., Lovell, J. E., & Preston, R. A. 1998, *ApJ*, 505, 928

Harrison, P. A., & Lyne, A. G. 1993, *MNRAS*, 265, 778

Issur, N. 2000, Ph.D. Dissertation, University of Mauritius

Johnston, S., Nicastro, L., & Koribalski, B. 1998, *MNRAS*, 297, 108

Lambert, H. C., & Rickett, B. J. 1999, *ApJ*, 517, 299

Lyne, A. G., & Smith, F. G. 1982, *Nature*, 298, 825

Lyne, A. G., & Graham-Smith, F. 1998, *Pulsar Astronomy*, (2nd ed.; Cambridge: Cambridge University Press)

Nicastro, L., & Johnston, S. 1995, *MNRAS*, 273, 122

Phillips, J. A., & Clegg, A. W. 1992, *Nature*, 360, 137

Roberts, J.A., & Ables, J.G. 1982, *MNRAS*, 201, 1119

Sandhu, J. S., Bailes, M., Manchester, R. N., Navarro, J., Kulkarni, S. R., & Anderson, S. B. 1997, *ApJ*, 478, L95

Smirnova, T. V., & Shabanova, T. 1992, *Soviet Astron.*, 36, 628

Stinebring, D. R., McLaughlin, M. A., Cordes, J. M., Becker, K. M., Espinoza Goodman, J. E., Kramer, M. A., Sheckard, J. L., & Smith, C. T. 2001, *ApJ*, 549, L97

Sutton, J.M., 1971, *MNRAS*, 155, 51

Taylor, J. H., & Cordes, J. M. 1993, *ApJ*, 411, 674

Taylor, J. H., Manchester, R. N., & Lyne, A. G. 1993, *ApJS*, 88, 529

Thompson, A. R., Moran, J. M., & Swenson, G. W., Jr. 1986, *Interferometry and Synthesis in Radio Astronomy*, (New York: John Wiley & Sons)

Toscano, M., Sandhu, J. S., Bailes, M., Manchester, R. N., Britton, M. C., Kulkarni, S. R., Anderson, S. B., & Stappers, B. W. 1999, *MNRAS*, 307, 925

Bibliography

Armstrong, J. W., & Rickett, B. J. 1981, *MNRAS*, 194, 623

Arons, J., & Barnard, J. J. 1986, *ApJ*, 302, 120

Backer, D. C. 1974, *ApJ*, 190, 667

Backer, D. C., Rankin, J. M., & Campbell, D. B. 1976, *Nature*, 263, 202

Barnard, J. J., & Arons, J. 1986, *ApJ*, 302, 138

Bell, J. F., Bailes, M., Manchester, R. N., Weisberg, J. M., & Lyne, A. G. 1995, *ApJ*, 440, L81

Beskin, V. S., Gurevich, A. V., & Istomin, I. N. 1988, *Ap&SS*, 146, 205

Bhat, N. D. R., Rao, A. P., & Gupta, Y. 1999, *ApJS*, 121, 483

Britton, M. C. 1996, Ph.D. Dissertation, University of California, Santa Barbara

Cheng, A. F., & Ruderman, M. A. 1979, *ApJ*, 229, 348

Cohen, M. H., & Cronyn, W. M. 1975, *ApJ*, 192, 193

Cordes, J. M. 1978, *ApJ*, 222, 1006

Cordes, J. M. 1986, *ApJ*, 311, 183

Cordes, J. M., & Wolszczan, A. 1986, *ApJ*, 307, L27

Cordes, J. M., Weisberg, J. M., & Boriakoff, V. 1985, *ApJ*, 288, 221

Desai, K. M., Gwinn, C. R., Reynolds, J. R., King, E. A., Jauncey, D., Flanagan, C., Nicolson, G., Preston, R. A., & Jones, D. L. 1992, *ApJ*, 393, L75

Fruchter, A. S. 1998, http://icarus.stsci.edu/~fruchter/nebula/nebula.html

Gallant, Y. A. 1996, in IAU Colloq. 160, *Pulsars: Problems and Progress*, ed. S. Johnston, M. A. Walker, & M. Bailes (San Francisco: Astronomical Society of the Pacific), 431

Goldreich, P. & Julian, W. H. 1969, *ApJ*, 157, 869

Gothoskar, P., & Gupta, Y. 2000, *ApJ*, 531, 345

Gupta, Y. 1995, *ApJ*, 451, 717

Gupta, Y., Rickett, B. J., & Lyne, A. G. 1994, *MNRAS*, 269, 1035

Gupta, Y., Bhat, N. D. R., & Rao, A. P. 1999, *ApJ*, 520, 173

Gwinn, C. R., Britton, M. C., Reynolds, J. E. J., Jauncey, D. L., King, E. A., McCulloch, P. M., Lovell, J. E., & Preston, R. A. 1998, *ApJ*, 505, 928

Gwinn, C. R., Britton, M. C., Reynolds, J. E. J., Jauncey, D. L., King, E. A., McCulloch, P. M., Lovell, J. E., Flanagan, C. S., & Preston, R. A. 2000, *ApJ*, 531, 902

Harrison, P. A., & Lyne, A. G. 1993, *MNRAS*, 265, 778

Issur, N. 2000, Ph.D. Dissertation, University of Mauritius

Johnston, S., Nicastro, L., & Koribalski, B. 1998, *MNRAS*, 297, 108

Komesaroff, M. M., Hamilton, P. A., & Ables, J. G. 1972, *Aust. J. Phys.*, 25, 759

Krishnamohan, S., & Downs, G. S. 1983, *ApJ*, 265, 372

Lambert, H. C., & Rickett, B. J. 1999, *ApJ*, 517, 299

Lee, L. C., & Jokipii, J. R. 1975, *ApJ*, 201, 532

Lerche, I. 1970, *ApJ*, 162, 153

Lyne, A. G., & Graham-Smith, F. 1998, *Pulsar Astronomy*, (2nd ed.; Cambridge: Cambridge University Press)

Lyne, A. G., & Smith, F. G. 1982, *Nature*, 298, 825

Lyutikov, M. 1998, Ph.D. Dissertation, California Institute of Technology

Macquart, J. P., Johnston, S., Walker, M., & Stinebring, D. 1999, in IAU Colloq. 177, *Pulsar Astronomy---2000 and Beyond*, ed. M. Kramer, N. Wex, & R. Wielebinski (San Francisco: Astronomical Society of the Pacific), 215

Manchester, R. N. 1975, *Proceedings of the Astronomical Society of Australia*, 2, 334

McKinnon, M. M., & Stinebring, D. R. 1998, *ApJ*, 502, 883

Melrose, D. B. 1996, in IAU Colloq. 160, *Pulsars: Problems and Progress*, ed. S. Johnston, M. A. Walker, & M. Bailes (San Francisco: Astronomical Society of the Pacific), 139

Nicastro, L., & Johnston, S. 1995, *MNRAS*, 273, 122

Phillips, J. A., & Clegg, A. W. 1992, *Nature*, 360, 137

Radhakrishnan, V., & Cooke, D. J. 1969, *Astrophys. Lett.*, 3, 225

Rankin, J. M. 1983, *ApJ*, 274, 333

Roberts, J.A., & Ables, J.G. 1982, *MNRAS*, 201, 1119

Sandhu, J. S., Bailes, M., Manchester, R. N., Navarro, J., Kulkarni, S. R., & Anderson, S. B. 1997, *ApJ*, 478, L95

Smirnova, T. V., & Shabanova, T. 1992, *Soviet Astron.*, 36, 628

Stinebring, D. R., McLaughlin, M. A., Cordes, J. M., Becker, K. M., Espinoza Goodman, J. E., Kramer, M. A., Sheckard, J. L., & Smith, C. T. 2001, *ApJ*, 549, L97

Sutton, J.M., 1971, *MNRAS*, 155, 51

Taylor, J. H., & Cordes, J. M. 1993, *ApJ*, 411, 674

Taylor, J. H., Manchester, R. N., & Lyne, A. G. 1993, *ApJS*, 88, 529

Thompson, A. R., Moran, J. M., & Swenson, G. W., Jr. 1986, *Interferometry and Synthesis in Radio Astronomy*, (New York: John Wiley & Sons)

Toscano, M., Sandhu, J. S., Bailes, M., Manchester, R. N., Britton, M. C., Kulkarni, S. R., Anderson, S. B., & Stappers, B. W. 1999, *MNRAS*, 307, 925